Effects of dispersed α-Al2O3 particles into a cold-sprayed aluminium coating on its subsequent oxidation by the PEO process

A. Maizeray, Grégory Marcos, Andrea Cappella, Marie-Pierre Planche, H. Liao, Gérard Henrion, Thierry Czerwiec, J. Martin

Effects of dispersed α-Al_2O_3 particles into a cold-sprayed aluminium coating on its subsequent oxidation by the PEO process

A. Maizeray[1,2], G. Marcos[1,2], A. Cappella[3], M.-P. Planche[4], H. Liao[4], G. Henrion[1,2], T. Czerwiec[1,2], J. Martin[1,2,*]

[1] Université de Lorraine, CNRS, IJL, F-54000 Nancy, France

[2] Université de Lorraine, Laboratoire d'Excellence Design of Alloy Metals for low-mass Structures ('LabEx DAMAS'), F-57045 Metz, France

[3] Université de Lorraine, CNRS, LEM3, Arts et Métiers ParisTech, F-57000 Metz, France

[4] Université de Technologie de Belfort Montbéliard, ICB, F-90400 Sevenans, France

*Corresponding author julien.martin@univ-lorraine.fr

Abstract

The present study focused on the use of a duplex surface treatment combining cold-spray deposition and plasma electrolytic oxidation (PEO) to produce an aluminium metal matrix composite coating, including dispersed α-Al_2O_3 particles, with improved tribological properties. Al/α-Al_2O_3 composite coatings were first deposited by cold-spray, with various thickness and proportion in α-Al_2O_3 particles, and, then partially oxidized by PEO under various processing durations and sparking regimes (arcs or soft regime). The feasibility of cold-spraying thick, compact and adherent aluminium coatings containing well-dispersed α-Al_2O_3 particles (up to 14 vol%) was demonstrated in this work. It was also pointed out that the addition of hard α-Al_2O_3 particles into the spray composition tends to densify the deposited aluminium coating. This was related to a stronger peening effect which, in turn, decreases the growth kinetic of the subsequent PEO oxide layer. The presence of dispersed α-Al_2O_3 particles was found to promote the formation of the corundum alumina phase in the PEO oxide layer by triggering the transition to the soft sparking regime earlier. It was also observed that dispersed α-Al_2O_3 particles remain unaffected throughout the PEO oxide layers formed within the conventional arcs sparking regime while they undergo a morphological transformation within the specific soft sparking regime. This was explained by considering the different type of micro-discharges that initiate during each regime. Finally, sliding wear tests revealed that the incorporation of α-Al_2O_3 particles into the cold-sprayed coating resulted in a slight decrease in the friction coefficient and the wear rate of the produced PEO layers.

Keywords

Cold-spray deposition; Plasma electrolytic oxidation (PEO); Aluminium; Alumina coating; soft sparking regime; Wear resistance

Highlights

- Dispersed α-Al_2O_3 particles decreases the growth kinetic of the PEO oxide layer.
- Dispersed α-Al_2O_3 particles triggers the PEO soft sparking regime earlier.
- Dispersed α-Al_2O_3 particles are differently affected depending on the PEO sparking regime.
- Dispersed α-Al_2O_3 particles slightly improves the wear properties of the PEO layer.

Graphical abstracts

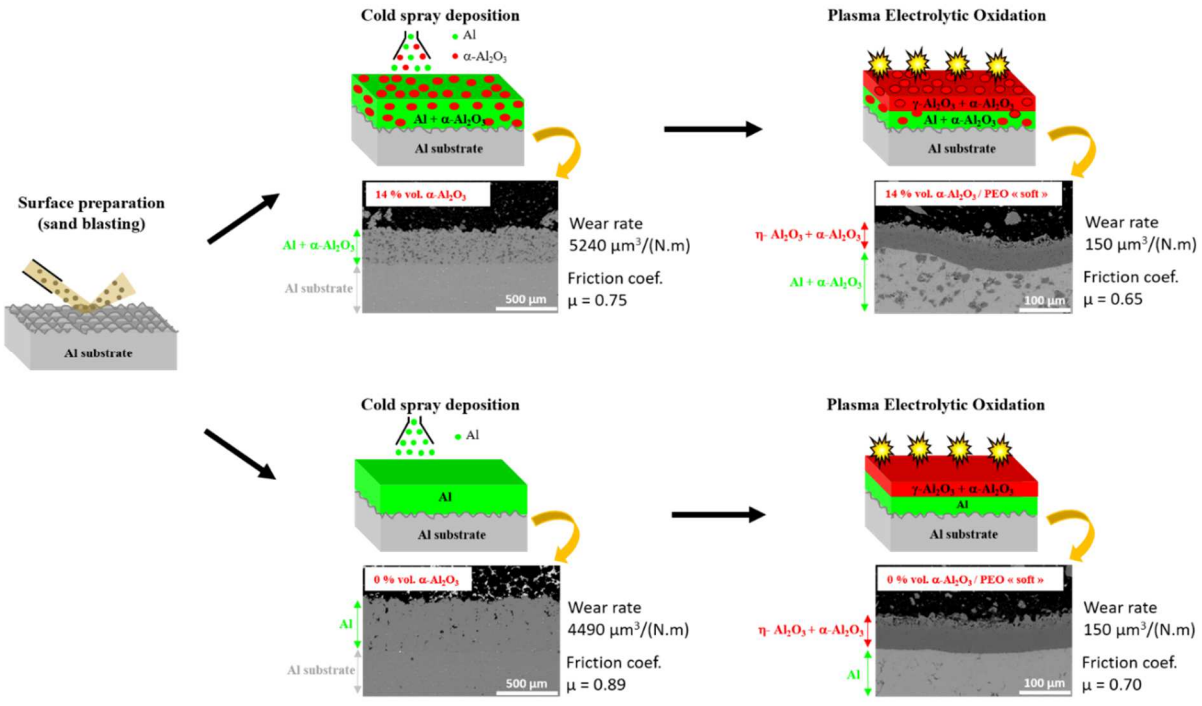

1. Introduction

In the field of advanced materials, metal matrix composites (MMC) occupy a prominent place [1]. They are composed of a metallic matrix reinforced by one or more other materials, generally ceramic, metallic or polymer particles. MMCs have improved mechanical, thermal and physical properties [2,3], making them useful in many potential applications such as aerospace components, like wings, fuselage, piston spacecraft exteriors rods to control nuclear radiation, automobile parts like brake disc, drum, and, solar-panels applications and in chemical reactions catalysts [1, 4, 5]. The leaders in MMC are aluminium metal matrix composites [1-5]. The main methods for preparing aluminium metal matrix composites are stir casting, liquid infiltration, powder metallurgy, spray deposition [6, 7]. Even if these technologies are promising, they have some drawbacks related to long production cycles, high costs and more important, the use of high processing temperatures. High temperatures can induce harmful interfacial reactions between metal and reinforcement particles resulting in a significant loss of the end-use properties of the composite material. Nowadays, the rapid development of cold-spraying technologies offers interesting perspectives for the preparation of relatively dense, thick and adherent aluminium-based MMCs coatings at the surface of various materials [7, 8]. This is due to the intrinsic ductility of aluminium that allows the plastic deformation of the powder and/or of the substrate to occur, which, in turn, promotes a mechanical bonding between the sprayed particles and the surface of the bulk material [9-12].

However, aluminium-based MMCs materials are sensitive to wear and corrosion, and additional surface treatments are usually applied to improve their surface properties. Treatments such as friction stir processing [13] or laser selective melting [14] have been implemented. Recently, plasma electrolytic oxidation (PEO) of MMCs has also been tested [15-18]. Plasma electrolytic oxidation (PEO), also referred to as micro-arc oxidation (MAO), is a plasma-assisted electrochemical conversion technique used to grow a protective oxide layer on

lightweight metals (*e.g.* Al, Mg, Ti) and their respective alloys [19-29]. Recent years have seen renewed interest for PEO to replace conventional concentrated acid anodizing processes. PEO process not only uses low concentrated alkaline electrolytes free of any toxic compounds, but also enables an improvement of the wear [30], corrosion [31, 32] and thermal resistance [33-35] of the produced oxide coatings. This makes this process attractive in different industrial domains such as transportation, building industry as well as biomedical engineering [36–38] and waste treatment [39, 40].

Rama Krishna and Sundararajan were the first to combine cold spray and PEO [41], followed by some other authors [42-45]. Tazegul et al. [44] obtained very good tribological characteristics of the duplex layers provided that the oxide layer formed by PEO does not reach the interface between the cold-spray layer and the substrate. Although aluminum coatings obtained by cold-spray remains more porous compared to bulk aluminium alloys, this can be advantageously exploited during post-PEO treatments. Indeed, Martin et al. showed that the growth kinetics of the oxide layers obtained by PEO are higher on a more porous sprayed aluminum coating than on denser aluminum substrates [45]. Other studies reported the co-deposition of aluminum with other particles to produce various MMCs coatings before carrying out PEO treatments [46-49]. Zhang et al. [46] showed that the presence of carbon nanotubes in the cold-sprayed coating improves the final friction properties of the PEO oxide layer. Rao et al. [47] obtained very interesting properties in abrasion dry sliding wear and corrosion for an alumina reinforced aluminum CS layer with a PEO treatment on AZ31 Mg alloy. Kuznetsov et al. [48] applied successfully such a duplex treatment on the bearing bores of electric motor bearing shields made of aluminum. Martin et al. [49] demonstrated the feasibility of the elaboration of alumina (Al_2O_3) - zirconia (ZrO_2) composite coatings on steel by combining cold-spray deposition and plasma electrolytic oxidation (PEO). Recently, Shao et al. [50] applied the same concept on a Ti6Al4V alloy by comparing the conventional arcs and the

particular soft sparking regimes of the PEO process. It was reported that PEO coatings produced within the soft regime exhibited a more compact structure, a relatively higher α-Al_2O_3 content, and a higher micro-hardness than that formed within the conventional arcs regime.

Jaspard-Mecuson et al. [51] pointed out an interesting feature of PEO that they named the soft sparking regime. Indeed, when using an AC current to supply the working electrode, a transition from the conventional arcs to the particular soft sparking regime can occur depending on the processing parameters, especially the ratio of anodic to cathodic charge quantity delivered to the electrodes [51, 52]. Transition to the soft regime is characterized by a gradual voltage drop [53, 54], as well as an acoustic attenuation[51, 54-56] and a decrease in light emission depending on the treated aluminum alloy [51, 54, 56]. Over the years, some factors have been identified to promote an earlier transition to the soft sparking regime: a higher current density or current frequency [57], a lower anodic to cathodic charge quantity ratio [56, 57, 59], the thickness of a pre-existing oxide layer [54] and ageing of the electrolyte [58]. Matykina et al. [54] conducted interesting PEO experiments under the soft regime when applied on pre-formed porous anodic films. They showed that the presence of such a film allows the soft regime to occur earlier in the course of the PEO treatment. However, the literature is not unanimous on the quality of the layers obtained using the soft regime. For some the growth rate is higher [51] while it is lower for others [56]. For flat substrates, and within conventional arcs conditions, the coating thickness is usually less at the center and thicker at the edge of the sample [60, 61]. However, the coating thickness was shown to be more spatially uniform within the soft sparking regime [52]. It is also usually observed that formation of high-temperature α-Al_2O_3 phase is favoured under the soft sparking regime while γ-Al_2O_3 phase dominates under the conventional arc sparking regime [62, 63]. Recently, the effect of black carbon and carbon nanotubes

incorporated into an aluminum PEO layer was shown to strongly affect the occurrence of the soft regime [64, 65].

The main motivation of this study was to apply the combination of cold-spray and plasma electrolytic oxidation (PEO) methods to develop resistant aluminium-based MMC coatings with dispersed alumina particles. The effects of these dispersed particles on the subsequent PEO process, within the arcs and soft sparking regimes, on the produced morphology and composition of the PEO oxide layers, and finally on the wearing properties of the produced duplex coatings were particularly explored.

2. Materials and methods

Figure 1 gives a schematic description of the duplex surface treatments carried out in the present study. A commercial 2017 grade aluminium alloy was used as metallic substrate (Table 1). The samples exhibited a square shape of $30 \times 30 \times 4$ mm^3. Only one large face of these samples was subjected to the duplex treatment, which represented a processed surface area of about 9 cm^2. The other faces were covered by a thermosetting resin. As depicted in figure 1, and prior to be cold-sprayed, surfaces were prepared by sandblasting with corundum particles under 6 bars pressure. It allows surface cleaning (*e.g.* removal of organic or oxide contaminations) and also provides a significant roughness ($R_a = 20\ \mu m \pm 5\ \mu m$) ensuring good adhesion of the cold-sprayed coating to the aluminium substrate.

A commercial 1050 grade aluminium (Table 2) and a commercially pure corundum α-Al_2O_3 (Table 3) powders were used for cold-spray depositions. The aluminium powder consisted of spherical particles with an average diameter of 30 ± 5 µm. The corundum powder consisted of small irregularly shaped Al_2O_3 pieces with an average size of $12\ \mu m \pm 5\ \mu m$. As summarized in table 4, mixtures of these two powders with various contents of corundum (0, 5

and 14 vol%) were co-sprayed onto the aluminium substrates. Spray duration was tuned in order to achieve coatings with thickness in the range 100 - 500 µm (Table 5). On this point, it can be noticed that a very thin cold-sprayed coating of about 70 µm with 5 vol% α-Al_2O_3 particles was produced on the substrate (sample CS5Al_2O_3 in tables 4 and 5) with the aim of specifically investigating the behavior of a duplex coating when the thickness of the PEO oxide layer becomes close to the one elaborated by cold-spray. All the cold-sprayed coatings were prepared using nitrogen as carrier gas with pressure and temperature parameters set to 28 bars and 340 °C, respectively. The spray-angle was 90° and the nozzle was set at 22 mm from the substrate. After cold-spray, a careful thinning was performed on the deposited coatings (polishing using SiC papers to diamond suspensions) in order to ensure the same surface finish for all samples (a mirror-like aspect with a roughness parameter R_a below 1 µm). A thickness less than 20 µm was removed during this polishing step.

These cold-sprayed coatings were then partially oxidized by carrying out PEO treatments using a homemade experimental set-up presented in detail in references [51, 52, 57]. PEO treatments were run in an alkaline electrolyte that consisted in a solution of anhydrous sodium silicate (1.65 $g \cdot L^{-1}$) and potassium hydroxide (1 $g \cdot L^{-1}$) diluted in deionized water. The resulting pH and electrical conductivity were measured at 12.5 and 7.5 $mS \cdot cm^{-1}$, respectively. The temperature of the electrolyte was maintained at 30 °C. In order to avoid a potential ageing of the electrolyte, a fresh one was used for each sample. A current generator was used to supply the aluminium sample and the titanium counter-electrodes. As depicted in figure 1 of a previous work [51], it provides an asymmetric quasi-squared bipolar pulse for which all the waveform parameters such as duration T_i, amplitude (anodic I_p and cathodic I_n), charge quantity (anodic Q_p and cathodic Q_n) of each pulse can be adjusted independently in a wide range. In the present study, the current pulse frequency, the anodic current density and the cathodic current density

were set at 100 Hz, 66 $A \cdot dm^{-2}$ and 39 $A \cdot dm^{-2}$, respectively. In addition, the ratio of the anodic to cathodic charge quantity was specifically set at 0.9, which allows the transition from the conventional arcs to the soft sparking regime to occur in the course of PEO treatments when performed on aluminium substrates [51, 52, 57]. As summarized in Table 4, some samples were PEO processed only under the arcs sparking regime for 20 min while other samples were PEO processed for 35 min, beyond the complete establishment of the soft sparking regime. After PEO, the treated samples were thoroughly rinsed with water, and cleaned with ethanol, and dried under a warm air stream. It is also worth mentioning that the electrical responses were recorded during each PEO treatment by using a 1 GHz bandwidth oscilloscope (Agilent Infiniium 54832B). From these recordings, the evolution of the anodic voltage amplitude with the PEO processing time was examined. For repeatability and reproducibility considerations, at least 3 samples were produced under each processing condition summarized in Table 4, and data given in Table 5 are the statistical result of measurements performed on each sample.

Produced samples were observed by SEM using a FEI Quanta 650 FEG working in backscattered electrons mode (BSE) for top-most surface and cross-section observations. SEM investigations were systematically done at the edge of the processed surfaces. For SEM observations, a thin carbon layer of about 10 nm in thickness was previously deposited on the observed surface of the samples in order to limit electrical charging effects. For the cross-section observations, the samples were previously cut and mounted in a thermosetting resin and finely polished to achieve a mirror-like aspect. The coating thickness of the as-sprayed and of PEO oxide coatings were then determined as an average value of 15 measures collected on SEM cross-section views over 2 different positions separated by a minimum distance of 500 µm. The porosity and the volume proportion of the sprayed α-Al_2O_3 particles in the coatings were quantitatively estimated by an image analysis procedure applied on the SEM cross-section

micrographs using ImageJ software. A minimum of 5 different views of about 300 µm × 300 µm in size were considered for this estimation and the resulting error bar corresponds to the standard deviation of the measurements. The phase composition of each investigated coating was determined by X-ray diffraction measurements (XRD) using a Bruker D8 ADVANCE instrument (Cu-$K_{\alpha 1}$ radiation $\lambda = 0.1542$ nm at 40 kV and 30 mA) and operating in the Bragg-Brentano geometry with a step size of 0.005° and a scan range from 30 to 85°. Finally, sliding wear tests were performed at room temperature under dry condition using the ball-on-disc test in the linearly reciprocating configuration (Anton-Paar TRN tribometer). The counterpart was a corundum ball with 6 mm diameter. The track length was 10 mm with a mean velocity of ~ 20 $mm \cdot s^{-1}$. Depending on the nature of the coating, the normal load and the sliding distance were adjusted as specified in table 5. For the as-sprayed coatings, consisting mainly of soft aluminium material, the normal load and the sliding distance were set at 1 N and 10 m, respectively. In contrast, for the PEO coatings composed of aluminium oxide, they were set at 7 N and 50 m, respectively. During each sliding test, the tangential load was measured, and the friction coefficient was calculated. Wear tracks were observed by optical microscopy and SEM (in secondary electron SE imaging mode) while the roughness profiles were recorded using an optical surfometer (GBS Smart WLI_extended). From these observations, the normalized wear rate was estimated using the MountainsMap® software.

3. Results and discussion

3.1 Cold-sprayed coatings

Figure 2 shows the cross-section SEM micrographs recorded at different magnifications on the as-sprayed samples CS0Al_2O_3 (Figure 2a) and CS14Al_2O_3 (Figure 2b). It can be observed that the α-Al_2O_3 particles are homogeneously distributed throughout the sprayed coating. They

also appear well incorporated into the sprayed aluminium matrix. A slight local disbound of about 1 µm in average can be observed between the sprayed α-Al_2O_3 and Al particles. Moreover, and whatever the processed sample, no evidence of delamination of the sprayed coating at the coating substrate interface was observed. It suggests that within the spraying conditions applied, the presence of 14 vol% of sprayed α-Al_2O_3 particles into the spray composition does not seem to affect the mechanical integrity of the deposited coating. Moreover, image analysis of the SEM micrographs evidenced that the coating porosity of the sample CS0Al_2O_3 was estimated at about 7 % while it is less than 0.5 % for the sample CS14Al_2O_3 (Figure 2 and Table 5). Meanwhile, the average thickness of the sprayed coating of sample CS0Al_2O_3 (420 ± 20 µm) is higher than that of the sample CS14Al_2O_3 (280 ± 20 µm) (Figure 2 and Table 5). It thus appears that the presence α-Al_2O_3 particles into the spray composition promotes more compact but thinner sprayed coatings. These observations can be explained by considering two concomitant effects of the α-Al_2O_3 particles when they are added with aluminium particles into the spray powder composition. Indeed, and as reported in the literature, the addition of denser (higher kinetic energy) and harder alumina particles (~ 3.95 $g \cdot cm^{-3}$ and ~ 1700 Hv, respectively) into the lighter-weight and softer Al powder (~ 2.7 $g \cdot cm^{-3}$ and ~ 50 Hv, respectively) helps densifying the sprayed coatings due to a more efficient peening of the surface [12, 66-69]. Meanwhile, the surface sputtering by heavy and hard particles is also more important, which limits the coating thickening and therefore decreases the overall growth kinetic.

Figure 3 shows the XRD diffraction patterns recorded on the samples CS0Al_2O_3 and CS14Al_2O_3. It confirms the exclusive presence of the fcc-Al structure in the aluminium sprayed coating (sample CS0Al_2O_3) and the combined presence of the fcc-Al and rhombohedral α-Al_2O_3 structures in the composite sprayed coating (sample CS14Al_2O_3). For the latter, intensity

of the α-Al_2O_3 alumina peaks is clearly lower compared with the intensity of the Al peaks which is in good agreement with the low amount of α-Al_2O_3 particles incorporated into the composite sprayed coating.

Figure 4 and table 5 report results from the dry sliding wear tests performed on the aluminum substrate and on the prepared cold-sprayed coatings with a normal load and a sliding distance set at 1 N and 10 m, respectively. As described in the experimental section, these wear tests were only carried out on the finely polished surface of the sprayed coatings. Figure 4 shows the variations of the friction coefficient as a function of the sliding distance for the samples CS0Al_2O_3 and CS14Al_2O_3. First, from a global point of view and whatever the amount of the dispersed α-Al_2O_3 particles, the average friction coefficient exhibits high amplitude fluctuations with the sliding distance suggesting adhesive and abrasive wear mechanisms. In addition, the average friction coefficient of sample CS14Al_2O_3 remains slightly lower than that of sample CS0Al_2O_3 (0.75 vs 0.89). This is particularly obvious for the first two sliding meters. Nevertheless, and as reported in table 5, the wear rate is higher for sample CS14Al_2O_3 ($7.0\times10^{-3} \pm 3\times10^{-4}$ $mm^3/(N\cdot m)$) than for sample CS0Al_2O_3 ($4.7\times10^{-3} \pm 4\times10^{-4}$ $mm^3/(N\cdot m)$). It can also be noticed that the friction coefficient and the wear rate measured on the unsprayed aluminum substrate (0.63 and $1.1\times10^{-3} \pm 4\times10^{-4}$ $mm^3/(N\cdot m)$, respectively) are lower than those measured for the cold-sprayed coatings. If they are in good agreement with results found by Arrabal et al. in the same wear test conditions, they also evidence that sprayed coatings have lower tribological properties mainly due to a lack of cohesion between sprayed particles compared to bulk material [106]. Figure 5 shows the 3D surface topography and the associated SEM micrographs of the wear tracks for the samples CS0Al_2O_3 (Figure 5a) and CS14Al_2O_3 (Figure 5b). A mix of abrasive and adhesive wear behaviour is observed which is in good agreement with the high amplitude variations of the friction coefficient as noticed in figure 4.

One can also note that it turns into a mostly abrasive behavior when adding α-Al_2O_3 particles. This is also confirmed by the presence of linear scratches in the wear track which puts in evidence a tree body erosion mechanism due to the presence of hard α-Al_2O_3 particles into the composite cold-sprayed coating (sample CS14Al_2O_3 in figure 5b). Finally, results from these wear tests suggest that the addition of α-Al_2O_3 particles into the aluminium sprayed coating has a beneficial effect on the friction coefficient by improving the dry lubrication property of the overall coating. Oppositely, their presence has a detrimental effect on the wear resistance of the aluminium coating because they promote abrasive mechanisms.

3.2 PEO treatments

Figure 6 shows the evolution of the anodic voltage amplitude as a function of the PEO processing time for the different duplex treatments summarized in Table 4. They reveal a quite similar trend whatever the composition of the cold-sprayed coatings. Over the first seconds of the process (~ 15 s), a thin barrier anodic film develops on the surface with a rapid increase in voltage (40 $V \cdot s^{-1}$) to maintain the current amplitude at a constant value. At this stage, no electrical discharges are observed while an intense gas release is visible all over the sample surface. The dielectric breakdown voltage of the growing barrier anodic film is then rapidly reached (~ 575 V) and small orange-red discharges initiate on the sample surface. From about 15 s to around 20 – 30 min, depending on the composition of the cold-sprayed coating, the PEO process runs under the arcs sparking regime during which the slope of the voltage-time curve reduces to about 0.07 $V \cdot s^{-1}$ and the micro-discharges gradually become bigger and fewer over the treated surface. Figure 6 shows that during this arcs sparking regime, the presence of dispersed α-Al_2O_3 particles in the sprayed aluminium coating has almost no influence, on either the anodic breakdown voltage or the anodic voltage amplitude. For longer PEO processing time a drop in the anodic voltage amplitude is observed at a process time that depends on the samples.

This voltage transition is concomitant with the transition from arcs to soft sparking regime. The micro-discharges then gradually turn into smaller size and shorter lifetime tiny discharges with a reduction of the optical and acoustic emissions [61, 70-72]. Figure 6 clearly shows that the incorporated α-Al_2O_3 particles into the aluminium sprayed coating influences the transition to the soft sparking regime. Without particles (sample CS0Al_2O_3_PEO35min), the soft regime occurs at about 27 min while it starts earlier at about 22 min with 14 vol% of dispersed α-Al_2O_3 particles (sample CS14Al_2O_3_PEO35min). This observation remains not clearly understood, but some identified parameters such as the chemical composition [61, 73-76] and the porosity [44, 54, 77, 78] of the treated material are known to affect the transition to the soft sparking regime and could explain the present experimental results.

3.3 PEO oxide coatings

Figure 7 shows cross-section and top-view SEM micrographs of the samples CS0Al_2O_3_PEO35min (Figure 7a) and CS14Al_2O_3_PEO35min (Figure 7b). For these two samples, the surface of the PEO coating consists entirely of a sponge-like morphology that is known to incorporate elements from the electrolyte (e.g. Si, Na, K), in its interconnected network of thin pores with diameters in the range of 0.1 – 1 µm [79, 80]. This sponge-like morphology is typical of PEO coatings grown within the soft sparking regime, which is in good agreement with the voltage-time responses shown in figure 6 [64, 81]. Moreover, figure 7 also evidences that the coating of sample CS0Al_2O_3_PEO35min is thicker than that of sample CS14Al_2O_3_PEO35min (72 ± 5 µm vs 57 ± 5 µm). This suggests that the presence of incorporated α-Al_2O_3 particles in the cold-sprayed aluminium coating tends to moderate the subsequent growth kinetic of the PEO coating. This can be explained by considering the differences in morphology between the as-sprayed coatings. Indeed, as established by Martin et al. in reference [45], the level of porosity has a very positive effect on the PEO growth kinetic.

This level being higher for the deposited Al coating without α-Al_2O_3 particles (~ 7 %) than for the Al/α-Al_2O_3 composite sprayed coating (< 0.5 %), it favors the growth of a thicker PEO oxide layer. Thus, the presence of hard α-Al_2O_3 particles in the spray composition tends to densify the sprayed coating due to a much more intense peening effect [12, 66-69], but consequently, it results in a thinner PEO oxide coating due to the low porosity level in the cold-sprayed coating. Figure 7 (and figures 9 and 10) also shows a more irregular interface between the PEO oxide layer and the cold-spray coating with dispersed α-Al_2O_3 particles (sample CS14Al_2O_3_PEO35min) compared to the one observed with the cold-spray coating containing no particle (sample CS0Al_2O_3_PEO35min). This can be explained by considering two hypothesis. First, and as mentioned in the experimental section, all the as-sprayed coatings were finely polished with the aim of eliminating the inherent roughness of cold-sprayed coatings by removing a thickness of about 20 µm. However, the sample containing a high amount of hard α-Al_2O_3 particles exhibited higher surface irregularities than for the other samples, that were probably not fully polished. After PEO, the subsequent oxide layer then followed these residual irregularities which could lead to a non-flat interface. Second, on the basis of studies dealing with PEO of bulk MMCs, Xue [18] and Liu et al. [16] established that large size SiC reinforced particles locally hinder growth of the PEO oxide layer while smaller size particles such as Al_2O_3-SiO_2 reinforced fibers are more rapidly transformed during the PEO treatment. The dispersed α-Al_2O_3 particles used in the present study having quite the same size than the SiC reinforced particles used in references [16, 18], it is also expected that they potentially hinder growth of the PEO oxide layer, and may locally result in a non-flat interface with the cold-sprayed MMC coating underneath

Figure 8 shows the X-ray diffraction patterns recorded on the PEO coatings of samples CS0Al_PEO35min and CS14Al_2O_3_PEO35min. As usually encountered for PEO of

aluminium, all coatings are predominantly composed of the crystalline aluminium oxides α- and γ-Al_2O_3 [82-84]. The presence of aluminium peaks is due to the incident X-ray beam that crosses the entire PEO coatings and reaches the aluminium cold-sprayed coatings underneath. Moreover, it can be observed that the relative intensity of α-Al_2O_3 and γ-Al_2O_3 peaks is largely higher for sample CS14Al_PEO35min than for sample CS0Al_PEO35min. Particularly, in the range of the scattering angles of 43-47°, some authors have proposed to use the relative intensity of (113) α-Al_2O_3 (at 43.6°) and (400) γ-Al_2O_3 (at 45.96°) peaks to judge on the relative proportion of α- and γ-alumina content and their variations in the overall layer phase composition [85, 86]. Figure 8 shows that this relative intensity of α- and γ-alumina peaks increases noticeably for sample CS14Al_PEO35min when compared with sample CS0Al_PEO35min. It suggests therefore that the presence of dispersed α-Al_2O_3 particles into the PEO processed material promotes the formation of the α-Al_2O_3 alumina phase during PEO. Nevertheless, it remains that a special attention must be paid to the analysis of the X-ray diffraction patterns. Indeed, for sample CS14Al_PEO35min, the intensity of the α-Al_2O_3 peaks is likely due to the joint contribution of the α-Al_2O_3 alumina phase produced during PEO and that of the residual α-Al_2O_3 sprayed particles into the produced PEO layer as well those lying underneath the PEO layer. This finally makes the quantification of the relative α-Al_2O_3 and γ-Al_2O_3 phase amount in the oxide layer by X-ray diffraction measurements in Bragg-Brentano geometry a complicated task.

Figure 9 compares the morphology of the PEO coatings produced on the samples CS14Al_2O_3_PEO20min (Figure 9a) and CS14Al_2O_3_PEO35min (Figure 9b). These samples contained the same amount of sprayed α-Al_2O_3 particles (14 vol%), but the first one was PEO processed for 20 min under the arcs sparking regime while the second was PEO processed for

35 min until the complete establishment of the soft sparking regime (Table 4 and Figure 6). In each case, the inward growth of the inner PEO sublayer and the outward growth of the outer one are indicated in figure 9. The original surface of the cold-spray coatings is close to the interface between the inner and the outer sublayers. Concerning the sample CS14Al_2O_3_PEO20min, the outer sublayer of the PEO oxide layer consists in a pancake-like morphology, which is typical of PEO coatings grown within the arcs sparking regime [87-91]. This structure consists in large and unfilled craters caused by strong electrical discharges that usually ignite over the processed surface during the arcs sparking regime [57, 92-94]. From the cross-section point of view, this structure appears as cracked plates that unevenly cover the topmost surface. This pancake-like morphology is clearly distinguishable from the finer sponge-like morphology observed in the outer sublayer of the oxide coating of the sample CS14Al_2O_3_PEO35min, which is typical of PEO coatings produced within the soft sparking regime. Figure 9 also shows that the PEO coating elaborated under the soft sparking regime is thicker and more homogeneous in thickness than the oxide coating produced under the arcs regime. This observation is in good agreement with previous works [51, 57]. More interestingly, and less commonly, figure 9 also highlights a major difference in the morphology of the inner sublayer of the PEO oxide coating between the samples CS14Al_2O_3_PEO20min and CS14Al_2O_3_PEO35min. Indeed, some sprayed α-Al_2O_3 particles are still distinguishable in the inner sublayer of the PEO coatings produced under the arcs sparking regime (Figure 9a). They are clearly recognizable by their typical angular and blocky morphology. They appear as non-affected by the PEO process, as if the advancing front of oxidation circumvented them. Oppositely, for the sample processed under the soft sparking regime, it is more difficult, even impossible, to detect these sprayed α-Al_2O_3 particles throughout the inner sublayer of the produced oxide (Figure 9b). One can observe some residual sprayed α-Al_2O_3 particles, but only

located at the interface between the cold-spray and the PEO coatings. In order to confirm this particular observation, figure 10 shows the cross-section (Figure 10a) and top-surface (Figure 10b) SEM micrographs recorded in a specific area of the sample CS14Al_2O_3_PEO20min where a juxtaposition of a sponge-like with a pancake-like morphology can be observed. First, it is important to remember that such a juxtaposition is commonly observed when the PEO process is about to switch from the arcs to the soft sparking regime, some locations over the processed surface undergoing the soft regime earlier and resulting in the formation of sponge-like morphologies locally. As a confirmation of previous observations, figure 10 shows again the presence of residual sprayed α-Al_2O_3 particles throughout the inner sublayer of the oxide coating, underneath the pancake-like morphology. In contrast, no sprayed α-Al_2O_3 particles are distinguishable inside the inner sublayer underneath the sponge-like morphology. Thus, it seems that within the soft sparking regime, the sprayed α-Al_2O_3 particles are strongly affected by the PEO process and they are gradually transformed into the same morphology than that observed for PEO of aluminium without particles incorporation.

The schematic illustration displayed in figure 11 shows the descriptive mechanism proposed to explain the gradual transformation of these dispersed α-Al_2O_3 particles during the transition from the arc to the soft PEO sparking regime. These explanations are mainly based on the existing models of discharge formation in the PEO process, especially the different types of micro-discharges that can appear through the specific bi-layered PEO oxide coating during each sparking regime [23, 24, 60, 73, 81, 92, 98, 99].

First, within the initial arc sparking regime (Figure 11a), and according to Hussein's model [81, 92, 98], strong B-type of discharges, originating from the metal-oxide interface, develop throughout the overall thickness of the PEO oxide coating, while softer A- and C-type discharges occur in micropores or cracks specifically located at the topmost surface of the

coating [81, 92, 98, 99] or throughout the overall coating [100-103] . The long-lived (> 100 µs) and large-sized (> 10 µm in average diameter) B-type discharges significantly affect the morphology of the coating and result in the formation of the typical cracked-pancake structures at the surface of the oxide coating as well as the formation of large cavities filled with electrolyte underneath the outer oxide sublayer [57, 58]. They are mainly responsible for the outward growth of the oxide coating as a result of the ejection of molten aluminium/alumina material from the heated discharge channel to the coating surface where it is rapidly solidified by the electrolyte [61, 81, 92, 98]. However, and although these intense B-type discharges dominate the arc sparking regime period of time, they occur fewer in number and less frequently compared to the smaller A and C-type micro-discharges [61, 98]. This is mainly due to a larger current "leakage" in each B-type discharge channel. Thus, the dispersed α-Al_2O_3 particles localized in the inner oxide sublayer are statistically less exposed to the surrounding detrimental B-type discharges, thereby limiting their morphological transformation. Add to that the fact that it is also well-established that presence of pores and structural defects significantly reduce the dielectric breakdown strength of alumina and favor its dielectric breakdown at lower voltage [95-97]. Micro-discharges are therefore expected to preferentially trigger through the micro-porous PEO alumina than across the denser dispersed α-Al_2O_3 particles, the latter exhibiting a higher dielectric breakdown strength. Thus, within the initial arc sparking regime, the B-type discharges circumvent in a major extend the sprayed α-Al_2O_3 particles, leaving them unaffected by the PEO process (see figures 9a and 10).

Secondly, with the transition from the arc to the soft sparking regime (Figure 11b), the intense and visible B-type discharges are gradually replaced by more numerous and tiny micro-discharges that remain confined in the micropores of the inner oxide sublayer [61, 81, 92, 98]. According to Cheng's model [23, 24, 60, 73, 99], they are classified as internal D-type micro-

discharges and they locally initiate between adjacent pores or cracks, as illustrated in figure 11b. It is now accepted that these short-lived (< 10 µs) and small-sized (< 1 µm in average diameter) D-type micro-discharges mainly lead to the inward growth of the microporous inner oxide sublayer. The oxidation growth front extends vertically towards the substrate and gradually overlaps the dispersed α-Al_2O_3 particles at the same time. As schematically described in the inset in figure 11b, and taking into account that dielectric breakdown is favored in porous and defect-full alumina, a D-type micro-discharge is most likely to initiate in the micro-porous alumina formed in the very closed vicinity of a dispersed α-Al_2O_3 particle. Thus, this particle locally undergoes a high mechanical stress (> 1 GPa [60]) due to shock-wave propagation as well as a significant increase in the temperature (> 3000 K [98, 104]). It leads to a local fragmentation, heating and melting of the interface of the dispersed α-Al_2O_3 particle followed by a solidification step when the micro-discharge extinguishes. In a recent study, Cheng et al. also evidenced the existence of higher temperature conditions in the inner PEO sublayer during the soft regime compared to the arc sparking one, which may significantly contributes to sinter and gradually transform the sprayed α-Al_2O_3 particles [62].

Finally, as the soft sparking regime goes on (Figure 11c), and with the repetitive ignition / extinction cycles of the surrounding D-type micro-discharges, the dispersed α-Al_2O_3 particles are gradually transformed into the typical micro-porous morphology of the inner PEO oxide sublayer, making them indistinguishable at the end of the PEO process (see figures 9b and 10).

Figure 12 and table 5 report results from the dry sliding wear tests performed on the prepared PEO oxide coatings with a normal load and a sliding distance set at 7 N and 50 m, respectively. More specifically, figure 12 shows the variations of the friction coefficient as a function of the sliding distance recorded on the samples CS0Al_2O_3_PEO35min and CS14Al_2O_3_PEO35min. Regardless of the α-Al_2O_3 particles content in the sprayed coating,

results clearly evidence an overall improvement of the tribological properties of the samples after PEO treatment (see figure 4 for comparison). First, the friction coefficient remains quite constant with the sliding distance for the PEO-treated samples while high amplitude fluctuations were observed for the as-sprayed samples. Secondly, for both samples, the calculated average friction coefficient is marked by a significant decrease after PEO treatment. It decreases from 0.89 to 0.70 after PEO treatment performed on the cold-sprayed coating containing no dispersed α-Al_2O_3 particles, while it reduces from 0.79 to 0.65 when PEO is applied on the deposited coating containing 14 vol% of sprayed α-Al_2O_3 particles. From these results, it also appears that the addition of α-Al_2O_3 particles into the sprayed coating slightly reduces the friction coefficient of the produced PEO layer from 0.70 to 0.65. This observation could be correlated by the relative content of the α-Al_2O_3 alumina phase in the PEO coatings as previously discussed with X-ray diffraction measurements (Figure 8). Indeed, they showed that a higher proportion of α-Al_2O_3 alumina phase is produced in the PEO coating that initially contained dispersed α-Al_2O_3 particles when compared with the one without sprayed α-Al_2O_3 particles. Thus, a higher content in α-Al_2O_3 alumina phase into the PEO layer, favoured by the initial dispersion of α-Al_2O_3 particles into the cold-sprayed coating, seems to contribute to reduce the friction coefficient of the synthesized duplex coating. This is in good agreement with previous studies [105-109].

As a complement of these sliding wear tests, figure 13 shows the 3D surface topographies and the associated SEM micrographs of the wear tracks for samples CS0Al_2O_3_PEO35min (Figure 13a) and CS14Al_2O_3_PEO35min (Figure 13b). By comparing figures 5 and 13, it clearly appears that the counter-body penetrates deeper in the pristine cold-sprayed coatings (CS0Al_2O_3 and CS14Al_2O_3) than in the PEO processed ones (CS0Al_2O_3_PEO35min and CS14Al_2O_3_PEO35min). This reveals that PEO treatment makes

the treated surfaces much more resistance to wear which is also confirmed by the calculated values of the wear rate. Indeed, and as reported in table 5, the wear rate of the PEO oxide layers is almost reduced by almost two orders of magnitude compared with the one measured on the cold-sprayed coatings. As usually observed for PEO of bulk aluminium substrate, the wear rate decreases from to $1.1\times10^{-3} \pm 4\times10^{-4}$ $mm^3/(N\cdot m)$ for the Al2017 substrate to $1.7\times10^{-5} \pm 5\times10^{-6}$ $mm^3/(N\cdot m)$ after PEO, these values being in good agreement with results found by Arrabal et al. in the same wear test conditions [106]. In addition, it is about $4.7\times10^{-3} \pm 4\times10^{-4}$ $mm^3/(N\cdot m)$ after cold-spray deposition (sample $CS0Al_2O_3$) and it drops down to about $2.4\times10^{-5} \pm 5\times10^{-6}$ $mm^3/(N\cdot m)$ after PEO treatment for 35 min ($CS0Al_2O_3$_PEO35min). It is worth noting that this achievement is all the more significant considering the severe wear test conditions used on the PEO oxide coatings (7 N normal force and 50 m sliding distance) compared with those applied on the as cold-sprayed coatings (1 N normal force and 10 m sliding distance). In addition, it appears that the depth of the wear tracks does not exceed 15 µm, which corresponds exactly to the thickness of the sponge-like outer sublayer of the PEO coatings elaborated within the soft sparking regime as shown in figure 9. SEM micrographs in figure 13 confirm that only the outermost sponge-like morphology was removed during the wear tests. These observations reveal that this sponge-like morphology is mechanically more brittle than the denser inner sublayer, hence making it more sensitive to abrasion. Regarding more specifically the PEO treated samples $CS0Al_2O_3$_PEO35min and $CS14Al_2O_3$_PEO35min, the wear tracks presented in figure 13 exhibit a similar aspect which reflects a fully abrasive wear mechanism. Thus, the wear mechanism evolves from a mixture of abrasive and adhesive behavior for the aluminium-based coatings deposited by cold-spray to a fully abrasive behavior for the alumina-based coatings produced after PEO. Finally, the dispersion of α-Al_2O_3 particles in the cold-sprayed coating does not seem to affect the wear mechanisms operating on the final duplex coatings.

3.4 Discussion about the conversion ratio of the sprayed coating into oxide

Figure 14a shows a cross-section SEM micrograph of sample CS5Al_2O_3_PEO35min. The PEO oxide layer exhibits the typical morphology of PEO coatings elaborated within the soft sparking regime, that is a thin and a nodular sponge-like morphology at the outermost surface, and a thicker and more compact inner sublayer. Surprisingly, transverse cracks are observed throughout the PEO oxide layer as well as delamination of the cold-sprayed coating at the interface with the aluminium substrate. Note that such morphological defects were not observed for the other samples that were PEO processed under the same conditions (CS0Al_2O_3_PEO35min and CS14Al_2O_3_PEO35min). This could be explained by considering the relative proportion of the oxide layer produced from the initial cold-sprayed coating. Indeed, for this specific sample CS5Al_2O_3_PEO35min, and as reminded in table 5, thickness of the cold-sprayed coating, is about 70 ± 10 µm which is thinner compared with the other sprayed coatings investigated in the present study (up to about 280 µm). After 35 min PEO processing time, the cross-section SEM micrograph in figure 14 shows that the thickness of the produced oxide layer is about 48 ± 5 µm, which is about 70 % of the sprayed coating thickness (compared to ~ 20 % for the samples CS0Al_2O_3_PEO35min and CS14Al_2O_3_PEO35min). For such a proportion of oxide, it is expected that the total strain experienced by the oxide layer, due to the building of thermal stress and stress generated by oxide formation and the associated volume expansion, cannot be accommodated further by the sprayed coating underneath. It results hence in the activation of damage mechanisms causing failures into the oxide layer and at the interface between the cold-spray coating and the aluminium substrate. Finally, the damaged morphology of this duplex coating has a detrimental effect on its tribological properties as shown in figure 14b and as summarized in table 5. Indeed, for the sample CS5Al_2O_3_PEO35min, the variation of the calculated friction coefficient as a function of the sliding distance exhibits higher

amplitude instabilities than for the sample CS14Al_2O_3_PEO35min. In addition, its average friction coefficient (0.73) and wear rate ($6.4\times10^{-5} \pm 5\times10^{-6}$ $mm^3/(N\cdot m)$ $\mu m^3/(N\cdot m)$) are also higher than for the other samples PEO processed under the same conditions. Finally, these last observations tend to demonstrate that the part of the metallic sprayed coating converted to oxide is of a crucial importance for the further development of high quality duplex aluminium MMC coatings produced by combining cold-spray and PEO methods.

4. Conclusion

In this study, the combination of cold-spray deposition and plasma electrolytic oxidation (PEO) methods was applied with the aim of producing composite ceramic coatings with improved tribological properties. More specifically, the influence of dispersed α-Al_2O_3 particles in a cold-sprayed aluminium coating (0, 5 and 14 vol%) on its subsequent oxidation by PEO (in arcs and soft sparking regimes) was questioned.

In the range of the cold-sprayed conditions investigated, the results collected on the as-cold-sprayed coatings support the following conclusions:

- The feasibility of cold-spraying thick (up to 280 µm), homogeneous and adherent aluminium-based coatings containing well-dispersed α-Al_2O_3 particles up to 14 vol% was demonstrated.
- The presence of hard α-Al_2O_3 particles into the spray promotes more compact but thinner coatings. This is due to concomitant opposite mechanisms: on one hand a larger peening effect reducing the porosity of the growing sprayed coating, and, on the other hand, a stronger sputtering effects limiting its thickening.
- Whatever the amount of dispersed α-Al2O3 particles, the as-sprayed coatings exhibit a poor tribological behaviour compared to bulk aluminium.

- The addition of α-Al_2O_3 particles in the aluminium sprayed coating has a beneficial effect on the friction coefficient by improving the dry lubrication property of the overall coating, but, in turn, decreases its wear behaviour.

The results collected on the duplex coatings, produced after PEO treatment on the as-sprayed coatings (in the range of the PEO conditions investigated), support the following conclusions:

- The dispersion of α-Al_2O_3 particles into the aluminium sprayed coating tends to moderate the growth kinetic of the PEO oxide layer. This is explained by the quite absence of porosity into the deposited coating, due to a strong peening effect of the sprayed hard particles.
- The dispersion of α-Al_2O_3 particles into the aluminium sprayed coating promotes the formation of the corundum phase during the post-PEO treatment because their presence triggers the transition to the PEO soft sparking regime earlier.
- Within the arcs sparking regime, the angular and blocky dispersed α-Al_2O_3 particles are not affected by the PEO process and keep their initial morphology. Oppositely, they are gradually transformed to a finely porous morphology within the soft sparking regime, making them unrecognizable throughout the PEO inner sublayer.
- PEO oxide coatings exhibit improved tribological properties compared with the as-sprayed coatings. The dispersion of α-Al_2O_3 particles into the aluminium sprayed coating slightly reduces the friction coefficient of the produced PEO coatings which can be attributed to a higher amount of corundum phase in the oxide layer.

Finally, based on the present work, further studies should be devoted to the development of composite ceramic coatings using zirconia or titania sprayed particles to achieve new tribological properties, and to get a better understanding of the transformation mechanisms of these dispersed particles during PEO. Similarly, for the further development of high quality

duplex aluminium MMC coatings produced by combining cold-spray and PEO methods, adhesion properties with the substrate should be assessed appropriately.

References

[1] B. Singh, I. Kumar, K.K. Saxena, K.A. Mohammed, M. Ijaz Khan, S. Ben Moussa, S.S. Abdullaev, A future prospects and current scenario of aluminium metal matrix composites characteristics, Alexandria Eng. J. 76 (2023) 1–17, https://doi.org/10.1016/j.aej.2023.06.028

[2] C.S. Kim, K. Cho, M.H. Manjili, M. Nezafati, Mechanical performance of particulate reinforced Al metal-matrix composites (MMCs) and Al Metal-Matrix Nano-Composites (MMNCs), J. Mater. Sci. 52 (2017) 13319–49, https://doi.org/10.1007/s10853-017-1378-x

[3] N.K. Bhoi, H. Singh H, S. Pratap, Developments in the aluminum metal matrix composites reinforced by micro/nano particles – a review, J. Compos. Mater. 54 (2020) 813–33, https://doi.org/10.1177/0021998319865307

[4] M.Y Khalid, R. Umer, K.A. Khan, Review of recent trends and developments in aluminium 7075 alloy and its metal matrix composites (MMCs) for aircraft applications, Res. Eng. 20 (2023) 101372, https://doi.org/10.1016/j.rineng.2023.101372

[5] J. Qadir, A.S Lewise, G.J.J. Wessley, G.D. Samuel, Influence of nanoparticles in reinforced aluminium metal matrix composites in aerospace applications – A review, Mater. Today – Proc. In Press (2023), https://doi.org/10.1016/j.matpr.2023.06.414

[6] P. Samal, P.R. Vundavilli, A. Meher, M.M. Mahapatra, Recent progress in aluminum metal matrix composites: A review on processing, mechanical and wear properties, J. Manuf. Process. 59 (2020) 131–152, https://doi.org/10.1016/j.jmapro.2020.09.010

[7] L. Zhao, N.H. Tariq, X. Cui, J. Wang, T. Xiong, Properties and research progress of cold-sprayed aluminum matrix composite coatings: a concise review, Heat Treat. Surf. Eng. 5 (2023) 2175528, https://doi.org/10.1080/25787616.2023.2175528

[8] A. Moridi, S. M. Hassani-Gangaraj, M. Guagliano, M. Dao, Cold spray coating: review of material systems and future perspectives, Surf. Eng. 30 (2014) 369-395, https://doi.org/10.1179/1743294414Y.0000000270

[9] H. Assadi, F. Gärtner, T. Stoltenhoff, H. Kreye, Bonding mechanism in cold gas spraying, Acta Mater. 51 (2003) 4379–4394, https://doi.org/10.1016/S1359-6454(03)00274-X

[10] P. Cavaliere, A. Silvello, Processing parameters affecting cold spay coatings performances, Int. J. Adv. Manuf. Technol. 71 (2014) 263–277

https://doi.org/10.1007/s00170-013-5465-0

[11] H. Assadi, H. Kreye, F. Gärtner, T. Klassen, Cold spraying - A materials perspective, Acta Mater. 116 (2016) 382-407, https://doi.org/10.1016/j.actamat.2016.06.034

[12] R.N. Raoelisona, Y. Xie, T. Sapanathan, M.P. Planche, R. Kromer, S. Costil, C. Langlade, Cold gas dynamic spray technology: A comprehensive review of processing conditions for various technological developments till to date, Addit. Manuf. 19 (2018) 134–159, https://doi.org/10.1016/j.addma.2017.07.001

[13] D.K. Sharma, V. Badheka, V. Patel, G. Upadhyay, Recent developments in hybrid surface metal matrix composites produced by friction stir processing: A Review, J. Tribol. 143 (2021) 050801, https://doi.org/10.1115/1.4049590

[14] M.P. Behera, T. Dougherty, S. Singamneni, K. De Silva, Selective laser melting of aluminium metal-matrix composites and the challenges, Mater. Today – Proc. 33 (2020) 5729–5733, https://doi.org/10.1016/j.matpr.2020.05.086

[15] R. Liu, N. Weng, W. Xue, M. Hua, G. Liud, W. Li, Analyses of reinforcement phases during plasma electrolytic oxidation on magnesium matrix composites, Surf. Coat. Technol. 269 (2015) 212–219, http://dx.doi.org/10.1016/j.surfcoat.2014.11.062

[16] C. Jiang, Y. Wang, S. Wang, Y. Zou, J. Ouyang, D. Jia, Y. Zhou, Effects of negative voltage on microstructure, electrical insulating, anti-corrosion, and thermal physical performance of plasma electrolytic oxidation coating on SiCp/Al composite, Appl. Surf. Sci. 636 (2023) 157789, https://doi.org/10.1016/j.apsusc.2023.157789

[17] L. Agureev, S. Savushkina, A. Ashmarin, A. Borisov, A. Apelfeld, K. Aniki, N. Tkachenko, M. Gerasimov, A. Shcherbakov, V. Ignatenko, N. Bogdashkina, Study of plasma electrolytic oxidation coatings on aluminum composites, Metals 8 (2018) 459,

https://doi:10.3390/met8060459

[18] W. Xue, Features of film growth during plasma anodizing of Al 2024/SiC metal matrix composite, Appl. Surf. Sci. 252 (2006) 6195-6200, https://doi.org/10.1016/j.apsusc.2005.08.029

[19] A.L. Yerokhin, X. Nie, A. Leyland, A. Matthews, S.J. Dowey, Plasma electrolysis for surface engineering, Surf. Coat. Technol. 122 (1999) 73–93, https://doi.org/10.1016/S0257-8972(99)00441-7

[20] P. Gupta, G. Tenhundfeld, E.O. Daigle, D. Ryabkov, Electrolytic plasma technology: Science and engineering - An overview, Surf. Coat. Technol. 201 (2007) 8746-8760, https://doi.org/10.1016/j.surfcoat.2006.11.023

[21] F. Simchen, M. Sieber, A. Kopp, T. Lampke, Introduction to Plasma Electrolytic Oxidation—An Overview of the Process and Applications, Coatings 10 (2020) 628, https://doi.org/10.3390/coatings10070628

[22] Gh. Barati Darband, M. Aliofkhazraei, P. Hamghalam, N. Valizade, Plasma electrolytic oxidation of magnesium and its alloys: Mechanism, properties and applications, J. Magnes. Alloy. 5 (2017) 74-132, https://doi.org/10.1016/j.jma.2017.02.004

[23] Y. L. Cheng, J. Cao, M. Mao, H. Xie, P. Skeldon, Key factors determining the development of two morphologies of plasma electrolytic coatings on an Al-Cu-Li alloy in aluminate electrolytes, Surf. Coat. Technol. 291 (2016) 239-249, https://doi.org/10.1016/j.surfcoat.2016.02.054

[24] Y.L. Cheng, J. Cao, Z. Peng, Q. Wang, E. Matykina, P. Skeldon, G.E. Thompson. Wear resistant coatings formed on Zircaloy-2 by plasma electrolytic oxidation in sodium aluminate electrolytes, Electrochim. Acta 116 (2014) 453-466, https://doi.org/10.1016/j.electacta.2013.11.079

[25] A. Mathis, E. Rocca, D. Veys-Renaux, J. Tardelli, Electrochemical behaviour of titanium in KOH at high potential, Electrochim. Acta 202 (2016) 253-261, https://doi.org/10.1016/j.electacta.2015.11.027

[26] D. Mashtalyar, K. Nadaraia, S. Sinebryukhov, S. Gnedenkov, Polymer-containing layers formed by PEO and spray coating method, Mater. Today : Proc. 11 (2019) 150-154, https://doi.org/10.1016/j.matpr.2018.12.123

[27] M.A. Khan, A.R. Safira, M. Aadil, M. Kaseem, Development of anti-corrosive coating on AZ31 Mg alloy modified by MOF/LDH/PEO hydrids, J. Mag. Alloys, In Press (2024), https://doi.org/10.1016/j.jma.2023.12.004

[28] S.V. Gnedenkov, S.L. Sinebryukhov, V.S Ergokin, I.E. Vyalyi, D.V. Mashtalyar, K.V. Nadaraia, D.K. Ryabov, V.M. Buznik, Formation and properties of composite coatings on aluminum alloys, Russ. J. Inorg. Chem. 62 (2017) 1-11, https://doi.org/10.1134/S0036023617010065

[29] I.G. Zhevtun, P.S. Gordienko, D.V. Mashtalyar, Y.N. Kulchin, S.B. Yarusova, V.A. Nepomnyushchaya, Z.E. Kornakova, S.S. Gribanova, D.V. Gritsuk, A.I. Nikitin, Tribological properties of Ti-TiC composite coatings on titanium alloys, Materials 15 (2022) 8941, https://doi.org/10.3390/ma15248941

[30] M. Molaei, K. Babaei, A. Fattah-Alhosseini, Improving the wear resistance of plasma electrolytic oxidation (PEO) coating applied on Mg and its alloys under the addition of nano- and micro-sized additives into the electrolytes: A review, J. Magnes. Alloy. 9 (2021) 1164-1186, https://doi.org/10.1016/j.jma.2020.11.016

[31] A. Buling, J. Zerrer, Increasing the application fields of magnesium by ultraceramic®: Corrosion and wear protection by plasma electrolytical oxidation (PEO) of Mg alloys, Surf. Coat. Technol. 369 (2019) 142-155, https://doi.org/10.1016/j.surfcoat.2019.04.025

[32] K. Ling, Q. Mo, X. Lv, G. Qin, W. Yang, L. Li, W. Li, Growth characteristics and corrosion resistance of micro-arc oxidation coating on Al-Mg composite plate, Vacuum 195 (2022) 110640, https://doi.org/10.1016/j.vacuum.2021.110640

[33] J.A. Curran, H. Kalkanci, Y. Magurova, T.W. Clyne, Mullite-rich plasma electrolytic oxide coatings for thermal barrier applications, Surf. Coat. Technol. 201 (2007) 8683-8687, https://doi.org/10.1016/j.surfcoat.2006.06.050

[34] Q. Xia, D. Zhang, D. Li, Z. Jiang, Z. Yao, Preparation of the plasma electrolytic oxidation coating on Mg-Li alloy and its thermal control performance, Surf. Coat. Technol. 369 (2019) 252-256, https://doi.org/10.1016/j.surfcoat.2019.04.073

[35] F. Muhaffel, M. Bayogan, H. Cimenoglu, A study to enhance the mechanical durability of the MAO coating fabricated on the 7075 Al alloy for wear-related high temperature applications, Surf. Coat. Technol. 409 (2021) 126843, https://doi.org/10.1016/j.surfcoat.2021.126843

[36] L.H. Li, Y.M. Kong, H.W. Kim, Y.W. Kim, H.E. Kim, S.J. Heo, J.Y. Koak, Improved biological performance of Ti implants due to surface modification by micro-arc oxidation, Biomater.25 (2004) 2867–2875, 10.1016/j.biomaterials.2003.09.048

[37] L. Pezzato, K. Brunelli, S. Diodati, M. Pigato, M. Bonesso, M. Dabalà, Microstructural and corrosion properties of hydroxyapatite containing PEO coating produced on AZ31 Mg alloy, Materials 14 (2021) 1531-1545, https://doi.org/10.3390/ma14061531

[38] L.V. Parfenova, E.S. Lukina, Z.R. Galimshina, G.U. Gil'fanova, V.R. Mukaeva, R.G. Farrakhov, K.V. Danilko, G.S. Dyakonov, E.V. Parfenov, Biocompatible organic coatings based on bisphosphonic acid RGD-derivatives for PEO-modified titanium implants, Molecules 25 (2020) 229-250, https://doi.org/10.3390/molecules25010229

[39] M. Coto, S.C. Troughton, P. Knight, R. Joshi, R. Francis, R.V. Kumar, T.W. Clyne, Optimization of the microstructure of TiO_2 photocatalytic surfaces created by Plasma Electrolytic Oxidation of titanium substrates, Surf. Coat. Technol. 411 (2021) 127000, https://doi.org/10.1016/j.surfcoat.2021.127000

[40] S. Stojadinović, N. Radić, N. Tadić R. Vasilić, B. Grbić, Enhanced ultraviolet light driven photocatalytic activity of ZnO particles incorporated by plasma electrolytic oxidation into Al_2O_3 coatings co-doped with Ce^{3+}, Opt. Mater. 101 (2020) 109768, https://doi.org/10.1016/j.optmat.2020.109768

[41] L.R. Krishna, G. Poshal, A. Jyothirmayi, G. Sundararajan, Compositionally modulated CGDS + MAO duplex coatings for corrosion protection of AZ91 magnesium alloy, J. Alloys Compd. 578 (2013) 355–361, http://dx.doi.org/10.1016/j.jallcom.2013.06.036

[42] R. Khanna, T. Kokubo, T. Matsushita, H. Takadama, Fabrication of dense α-alumina layer on Ti-6Al-4V alloy hybrid for bearing surfaces of artificial hip joint, Mater. Sci. Eng., C 69 (2016) 1229–1239, https://doi.org/10.1016/j.msec.2016.08.025

[43] Z. Jing, K. Dejun, Effect of micro arc oxidation on micro – structure and electrochemical corrosion performance of cold sprayed aluminum coating, Anti-Corros. Methods Mater. 65 (2018) 572-579, https://doi.org/10.1108/ACMM-05-2018-1942

[44] O. Tazegul, F. Muhaffel, O. Meydanoglu, M. Baydogan, E.S. Kayali, H. Cimenoglu, Wear and corrosion characteristics of novel alumina coatings produced by micro-arc oxidation on AZ91D magnesium alloy, Surf. Coat. Technol. 258 (2014) 168–173, http://dx.doi.org/10.1016/j.surfcoat.2014.09.035

[45] J. Martin, K. Akoda, V. Ntomprougkidis, O. Ferry, A. Maizeray, A. Bastien, P. Brenot, G. Ezo'o, G. Henrion, Duplex surface treatment of metallic alloys combining cold-spray and plasma electrolytic oxidation, technologies, Surf. Coat. Technol. 392 (2020) 125756, https://doi.org/10.1016/j.surfcoat.2020.125756

[46] Y. Zhang, Q. Wang, R. Ye, C.S. Ramachandran, Plasma electrolytic oxidation of cold spray kinetically metallized CNT-Al coating on AZ91-Mg alloy: Evaluation of mechanical and

surficial characteristics, J. Alloys Compd. 892 (2021) 162094, https://doi.org/10.1016/j.jallcom.2021.162094

[47] Y. Rao, Q. Wang, J. Chen, C.S. Ramachandran, Abrasion, sliding wear, corrosion, and cavitation erosion characteristics of a duplex coating formed on AZ31 Mg alloy by sequential application of cold spray and plasma electrolytic oxidation techniques, Mater. Today Commun. 26 (2021) 101978, https://doi.org/10.1016/j.mtcomm.2020.101978

[48] Y. Kuznetsov, I. Kravchenko, D. Gerashchenkov, M. Markov, V. Davydov, A. Mozhayko, V. Dudkin, A. Bykova, The use of cold spraying and micro-arc oxidation techniques for the repairing and wear resistance improvement of motor electric bearing shields, Energies 15 (2022) 912, https://doi.org/10.3390/en15030912

[49] J. Martin, A. Maizeray, C. Da Silva Tousch, G. Marcos, T. Czerwiec, G. Henrion, A new strategy to prepare alumina-zirconia composite or multi-layered coatings by combining cold-spray deposition and plasma electrolytic oxidation, Mater. Today Commun. 36 (2023) 106676, https://doi.org/10.1016/j.mtcomm.2023.106676

[50] M. Shao, W. Wang, H. Yang, X. Zhang, X. He, Preparation of Wear-Resistant Coating on Ti6Al4V Alloy by Cold Spraying and Plasma Electrolytic Oxidation, Coatings 11 (2021) 1288, https://doi.org/10.3390/coatings11111288

[51] F. Jaspard-Mécuson, T. Czerwiec, G. Henrion, T. Belmonte, L. Dujardin, A. Viola, J. Beauvir, Tailored aluminium oxide layers by bipolar current adjustment in the Plasma Electrolytic Oxidation (PEO) process, Surf. Coat. Technol. 201 (2007) 8677–8682, https://doi.org/10.1016/j.surfcoat.2006.09.005

[52] A. Melhem, G. Henrion, T. Czerwiec, J.L. Briançon, T. Duchanoy, F. Brochard, T. Belmonte, Changes induced by process parameters in oxide layers grown by the PEO process on Al alloys, Surf. Coat. Technol. 205 (2011) S133–S136, https://doi.org/10.1016/j.surfcoat.2011.01.046

[53] E. Matykina, R. Arrabal, P. Skeldon, G.E. Thompson, Investigation of the growth processes of coatings formed by AC plasma electrolytic oxidation of aluminium, Electrochim. Acta 54 (2009) 6767-6778, https://doi.org/10.1016/j.electacta.2009.06.088

[54] E. Matykina, R. Arrabal, P. Skeldon, G.E. Thompson, P. Belenguer, AC PEO of aluminium with porous alumina precursor films, Surf. Coat. Technol. 205 (2010) 1668–1678, https://doi.org/10.1016/j.surfcoat.2010.05.014

[55] A. I. Slonova, O. P. Terleeva, Morphology, structure, and phase composition of microplasma coatings formed on Al-Cu-Mg alloy, Prot. Met. 44 (2008) 65-75, https://doi.org/10.1134/S0033173208010098

[56] W. Gebarowski, S. Pietrzyk, Influence of the cathodic pulse on the formation and morphology of oxide coatings on aluminium produced by plasma electrolytic oxidation, Metall. Mater. 58 (2013) 241–245, https://doi.org/10.2478/v10172-012-0180-7

[57] J. Martin, A. Melhem, I. Shchedrina, T. Duchanoy, A. Nominé, G. Henrion, T. Czerwiec, T. Belmonte, Effects of electrical parameters on plasma electrolytic oxidation of aluminium, Surf. Coat. Technol. 221 (2013) 70-76 , https://doi.org/10.1016/j.surfcoat.2013.01.029

[58] J. Martin, P. Leone, A. Nominé, D. Veys-Renaux, G. Henrion, T. Belmonte, Influence of electrolyte ageing on the Plasma Electrolytic Oxidation of aluminium, Surf. Coat. Technol. 269 (2015) 36–46, https://doi.org/10.1016/j.surfcoat.2014.11.001

[59] Y. Cheng, T. Feng, Y. Cheng, A systematic study of the role of cathodic polarization and new findings on the soft sparking phenomenon from plasma electrolytic oxidation of an Al-Cu-Li alloy, J. Electrochem. Soc. 169 (2022) 071505, https://doi.org/10.1149/1945-7111/ac82cc

[60] T. W. Clyne, S.C. Troughton, A review of recent work on discharge characteristics during plasma electrolytic oxidation of various metals, Int. Mater. Rev. 64 (2019) 127-162, https://doi.org/10.1080/09506608.2018.1466492

[61] D.S. Tsai, C.C. Chou, Review of the soft sparking issues in plasma electrolytic oxidation, Metals 8 (2018) 105, https://doi.org/10.3390/met8020105

[62] X. He, T. Feng, Y. Cheng, P. Hu, Z. Le, Y. Cheng, Fast formation of a black inner α-AL2O3 layer doped with CuO on Al-Cu-Li by soft sparking PEO process, J. Amer. Ceram. Soc. 106 (2023) 7019-7042, https://doi.org/10.1111/jace.19240

[63] E. Bousser, A; Rogov, P. Shashkov, A. Gholinia, N. Laugel, T. J.A. Slater, P.J. Withers, A; Matthews, A. Yerokhin, Phase transition in alumina films during post-sparking anodising of Al alloys, Acta Mater. 244 (2023) 118587, https://doi.org/10.1016/j.actamat.2022.118587

[64] L. Magniez, C. Da Silva Tousch, S. Fontana, J. Martin, T. Czerwiec, C. Hérold, G. Henrion, How carbon black nanoparticles affect the occurrence of soft-sparking during plasma electrolytic oxidation, Mater. Lett. 350 (2023) 134960, https://doi.org/10.1016/j.matlet.2023.134960

[65] C. Da Silva Tousch, L. Magniez, S. Fontana, G. Marcos, C. Hérold, G. Henrion, T. Czerwiec, J. Martin, Influence of carbon nanotubes on the plasma electrolytic oxidation process of aluminum under "soft" sparking conditions Surf. Coat. Technol. 468 (2023) 129779, https://doi.org/10.1016/j.surfcoat.2023.129779

[66] K. Spencer, D.M. Fabijanic, M.X. Zhang, The use of Al–Al_2O_3 cold spray coatings to improve the surface properties of magnesium alloys, Surf. Coat. Technol. 204 (2009) 336–344, https://doi.org/10.1016/j.surfcoat.2009.07.032

[67] Y. Tao, T. Xiong, C. Sun, H. Jin, H. Du, T. Li, Effect of α-Al_2O_3 on the properties of cold sprayed Al/α-Al_2O_3 composite coatings on AZ91D magnesium alloy, Appl. Surf. Sci. 256 (2009) 261–266, https://doi.org/10.1016/j.apsusc.2009.08.012

[68] Q. Wang, K. Spencer, N. Birbilis, M.X. Zhang, The influence of ceramic particles on bond strength of cold spray composite coatings on AZ91 alloy substrate, Surf. Coat. Technol. 205 (2010) 50–56, https://doi.org/10.1016/j.surfcoat.2010.06.008

[69] M. Jeandin, G. Rolland, L. L. Descurninges, M. H. Berger, Which powders for cold spray?, Surf. Eng. 30 (2014) 291-298, https://doi.org/10.1179/1743294414Y.0000000253

[70] E. Matykina, R. Arrabal, A. Pardo, M. Mohedano, B. Mingo, I. Rodriguez, J. González, Energy-efficient PEO process of aluminium alloys, Mat. Lett. 127 (2014) 13-16, https://doi.org/10.1016/j.matlet.2014.04.077

[71] V. Ntomprougkidis, J. Martin, A. Nominé, G. Henrion, Sequential run of the PEO process with various pulsed bipolar current waveforms, Surf. Coat. Technol. 374 (2019) 713-724, https://doi.org/10.1016/j.surfcoat.2019.06.057

[72] M. Kaseem, S. Fatimah, N. Nashrah, Y.G. Ko, Recent progress in surface modification of metals coated by plasma electrolytic oxidation: principle, structure, and performance, Prog. Mater. Sci 117 (2021) 100735, https://doi.org/10.1016/j.pmatsci.2020.100735

[73] Y.L. Cheng, Z.G. Xue, Q. Wang, X.Q. Wu, E. Matykina, P. Skeldon, G.E. Thompson, New findings on properties of plasma electrolytic oxidation coatings from study of an Al-Cu-Li alloy, Electrochim. Acta 107 (2013) 358-378, https://doi.org/10.1016/j.electacta.2013.06.022

[74] X. Lu, M. Mohedano, C. Blawert, E. Matykina, R. Arrabal, K.U. Kainer, M.L. Zheludkevich, Plasma electrolytic oxidation coatings with particle additions – A review, Surf. Coat. Technol. 307 (2016) 1165-1182, https://doi.org/10.1016/j.surfcoat.2016.08.055

[75] F. Tjiang, L.W. Ye, Y.J. Huang, C.C. Chou, D.S. Tsai, Effect of processing parameters on soft regime behaviour of plasma electrolytic oxidation of magnesium, Ceram. Int. 43 (2017) S567-S572, https://doi.org/10.1016/j.ceramint.2017.05.179

[76] C. Jiang, Y. Wang, S. Wang, Y. Li, Y. Zou, J. Ouyang, D. Jia, Y. Zhou, Achieving high-efficiency electrically insulating ceramic layer formed on SiCp/Al composite by bipolar pulsed PEO for novel integrated strategy, Surf. Coat. Technol. 444 (2022) 128692, https://doi.org/10.1016/j.surfcoat.2022.128692

[77] E. Matykina, R. Arrabal, A. Mohamed, P. Skeldon, G.E. Thompson, Plasma electrolytic oxidation of pre-anodized aluminium, Corros. Sci. 51 (2009) 2897-2905, https://doi.org/10.1016/j.corsci.2009.08.004

[78] W. Gong, R. Ma, A. Du, X. Zhao, Y. Fan, The effects of the pre-anodized film thickness on growth mechanism of plasma electrolytic oxidation coatings on the 1060 Al substrate, Materials 16 (2023) 5922, https://doi.org/10.3390/ma16175922

[79] K. Tillous, T. Toll-Duchanoy, E. Bauer-Grosse, L. Hericher, G. Geandier, Microstructure and phase composition of microarc oxidation surface layers formed on aluminium and its alloys 2214-T6 and 7050-T74, Surf. Coat. Technol. 203 (2009) 2969-2973, https://doi.org/10.1016/j.surfcoat.2009.03.021

[80] J. Martin, A. Nominé, V. Ntomprougkidis, S. Migot, S. Bruyère, F. Soldera, T. Belmonte, G. Henrion, Formation of a mestastable nanostructured mullite during Plasma Electrolytic Oxidation of aluminium in “soft” regime condition, Mater. Design 180 (2019) 107977, https://doi.org/10.1016/j.matdes.2019.107977

[81] R.O. Hussein, X. Nie, D.O. Northwood, Influence of process parameters on electrolytic plasma discharging behavior and aluminium oxide coating microstructure, Surf. Coat. Technol. 205 (2010) 1659-1667, https://doi.org/10.1016/j.surfcoat.2010.08.059

[82] A.L. Yerokhin, A. Shatrov, V. Samsonov, P. Shashkov, A. Pilkington, A. Leyland, A. Matthews, Oxide ceramic coatings on aluminium alloys produced by a pulsed bipolar plasma electrolytic oxidation process, Surf. Coat. Technol. 199 (2005) 150-157, https://doi.org/10.1016/j.surfcoat.2004.10.147

[83] J.A. Curran, T.W. Clyne, Thermo-physical properties of plasma electrolytic oxide coatings on aluminium, Surf. Coat. Technol. 199 (2005) 168-176, https://doi.org/10.1016/j.surfcoat.2004.09.037

[84] R.H.U. Khan, A. Yerokhin, X. Li, H. Dong, A. Matthews, Surface characterization of DC plasma electrolytic oxidation treated 6082 aluminium alloy : Effect of current density and electrolyte concentration, Surf. Coat. Technol. 205 (2010) 1679-1688, https://doi.org/10.1016/j.surfcoat.2010.04.052

[85] W. Xue, Z. Deng, Y. Lai, R. Chen, Analysis of phase distribution for ceramic coatings formed by microarc oxidation on aluminium alloy, J. Am. Ceram. Soc. 81 (1998) 1365-1368, https://doi.org/10.1111/j.1151-2916.1998.tb02493.x

[86] A.L. Yerokhin L.O. Snizhko, N.L. Gurevina, A. Leyland, A. Pilkington, A. Matthews, Discharge characterization in plasma electrolytic oxidation of aluminium, J. Phys. D: Appl. Phys. 36 (2003) 2110-2120, https://doi.org/10.1088/0022-3727/36/17/314

[87] G. Sundararajan, L. Rama Krishna, Mechanisms underlying the formation of thick alumina coatings through the MAO coating technology, Surf. Coat. Technol. 167 (2003) 269-277, https://doi.org/10.1016/S0257-8972(02)00918-0

[88] S.C. Troughton, A. Nominé, J. Dean, T.W. Clyne, Effect of individual discharge cascades on the microstructure of plasma electrolytic oxidation coatings, Appl. Surf. Sci. 389 (2016) 260-269, https://doi.org/10.1016/j.apsusc.2016.07.106

[89] E. Erfanifar, M. Aliofkhazraei, H.F. Nabavi, H. Sharifi, A.S. Rouhaghdam, Growth kinetics and morphology of plasma electrolytic oxidation coating on aluminium, Mater. Chem. Phys. 185 (2017) 162-175, https://doi.org/10.1016/j.matchemphys.2016.10.019

[90] Y.K. Wu, Z. Yang, R.Q. Wang, G.R. Wu, D. Chen, D.D. Wang, X.T. Liu, D.L. Li, C.H. Guo, S.X. Yu, D.J. Shen, P. Nash, An investigation of microstructure evolution for plasma electrolytic oxidation (PEO) coated Al in an alkaline silicate electrolyte, Surf. Coat. Technol. 351 (2018) 136-152, https://doi.org/10.1016/j.surfcoat.2018.07.055

[91] J. Martin, P. Haraux, V. Ntomprougkidis, S. Migot, S. Bruyère, G. Henrion, Characterization of metal oxide micro/nanoparticles elaborated by plasma electrolytic oxidation of aluminium and zirconium alloys, Surf. Coat. Technol. 397 (2020) 125987, https://doi.org/10.1016/j.surfcoat.2020.125987

[92] R.O. Hussein, D.O. Northwood, X. Nie, Coating growth behavior during the plasma electrolytic oxidation process, J. Vac. Sci. Technol. A 28 (2010) 766-773, https://doi.org/10.1116/1.3429583

[93] R.O. Hussein, X. Nie, D.O. Northwood, An investigation of ceramic coating growth mechanisms in plasma electrolytic oxidation (PEO) processing, Electrochim. Acta, 112 (2013) 111-119, https://doi.org/10.1016/j.electacta.2013.08.137

[94] A. Nominé, S.C. Troughton, A.V. Nominé, G. Henrion, T.W. Clyne, High speed video evidence for localized discharge cascades during plasma electrolytic oxidation, Surf. Coat. Technol. 269 (2015) 125-130, https://doi.org/10.1016/j.surfcoat.2015.01.043

[95] M. Touzin, D. Goeuriot, H.J. Fitting, C. Guerret-Piécourt, D. Juvé, D. Tréheux, Relationships between dielectric breakdown resistance and charge transport in alumina materials – Effects of the microstructure, J. Europ. Ceram. Soc. 27 (2007) 1193-1197, https://doi.org/10.1016/j.jeurceramsoc.2006.05.047

[96] T. Zhang, Y. Lei, J. Yin, J. Du, P. Yu, Effects of pores on dielectric breakdown of alumina ceramics under AC electric field, Ceram. Int. 45 (2019) 13951-13957, https://doi.org/10.1016/j.jeurceramsoc.2020.03.024

[97] T. Zhang, J. Du, Y. Lei, Y. Cheng, W. Liu, X. Yi, J. Yin, P. Yu, Effect of pores on dielectric breakdown strength of alumina ceramics via surface and volume effects, J. Europ. Ceram. Soc. 40 (2020) 3019-3026, https://doi.org/10.1016/j.jeurceramsoc.2020.03.024

[98] R.O. Hussein, X. Nie, D.O. Northwood, A. Yerokhin, A. Matthews, Spectroscopic study of electrolytic plasma and discharging behavior during the plasma electrolytic oxidation (PEO) process. J. Phys. D : Appl. Phys. 43 (2010) 105203, https://doi.org/10.1088/0022-3727/43/10/105203

[99] W. Tu, Y. Cheng, X. Wang, T. Zhan, J. Han, Y. Cheng, Plasma electrolytic oxidation of AZ31 magnesium alloy in aluminate-tungstate electrolytes and the coating formation mechanism, J. Alloys Comp. 725 (2017) 199-216, https://doi.org/10.1016/j.jallcom.2017.07.117

[100] Wang, H. Tang, R. Wang, Y. Tan, H. Zhang, S. Peng, Cathodic voltage-dependent composition, microstructure and corrosion resistance of plasma electrolytic oxidation coatings formed on Zr-4 alloy, RSC adv. 6 (2016) 34616, https://doi.org/10.1039/C6RA06197D

[101] R. liu, J. Wu, W. Xue, Y. Qu, C. Yang, B. Wang, X. Wu, Discharge behaviors during plasma electrolytic oxidation on aluminum alloy, Mater. Chem. Phys. 148 (2014) 284-292, https://doi.org/10.1016/j.matchemphys.2014.07.045

[102] X. Liu, G. li, Y. Xia, Investigation of the discharge mechanism of plasma electrolytic oxidation using Ti tracer, Surf. Coat. Technol. 206 (2012) 4462-4465, https://doi.org/10.1016/j.surfcoat.2012.05.002

[103] F. Gao, L. Hao, G. Li, Y. Xia, The plasma electrolytic oxidation micro-discharge channel model and its microstructure characteristic based on Ti tracer, Appl. Surf. Sci. 431 (2018) 13-16, https://doi.org/10.1016/j.apsusc.2017.07.281

[104] J. Martin, A. Nominé, F. Brochard, J.L. Briançon, C. Noël, T. Belmonte, T. Czerwiec, G. Henrion, Delay in micro-discharges appearance during PEO of Al: Evidence of a mechanism of charge accumulation at the electrolyte /oxide interface, Appl. Surf. Sci. 410 (2017) 29-41, https://doi.org/10.1016/j.apsusc.2017.03.088

[105] V.N. Malyshev, K.M. Zorin, Features of microarc oxidation coatings formation technology in slurry electrolytes, Appl. Surf. Sci. 254 (2007) 1511-1516, https://doi.org/10.1016/j.apsusc.2007.07.079

[106] R. Arrabal, M. Mohedano, E. Matykina, A. Pardo, B. Mingo, M.C. Merino, Characterization and wear behavior of PEO coatings on 6082-T6 aluminium alloys with incorporated α-Al_2O_3 particles, Surf. Coat. Technol. 269 (2015) 64-73, https://doi.org/10.1016/j.surfcoat.2014.10.048

[107] H.J. Xie, Y.L. Cheng, S.X. Li, J.H. Cao, L. Cao, Wear and corrosion resistant coatings on surface of cast A356 aluminium alloy by plasma electrolytic oxidation in moderately concentrated aluminate electrolytes, Trans. Nonferrous Met. Soc. China 27 (2017) 336-351, https://doi.org/10.1016/S1003-6326(17)60038-4

[108] M. Ghafaripoor, K. Raeissi, M. Santamaria, A. Hakimizad, The corrosion and tribocorrosion resistance of PEO composite coatings containing α-Al_2O_3 particles on 7075 Al alloy, Surf. Coat. Technol. 349 (2018) 470-479,

https://doi.org/10.1016/j.surfcoat.2018.06.027

[109] Y. Zhang, W. Fan, H.Q. Du, Y.W. Zhao, Microstrutcure and wearing properties of PEO coatings: Effects of Al_2O_3 and TiO_2, Surf. Rev. Lett. 25 (2018) 1850102, https://doi.org/10.1142/S0218625X18501020

Acknowledgments

- This work was supported by the French Government through the programme "Investissements d'avenir" operated by l'agence nationale de la recherche (ANR) and referenced to as ANR-11-LABX-0008-01 ('LabEx DAMAS').
- The authors would like to acknowledge the Conseil Régional de la Région Grand Est for granting C. Da Silva Tousch's under decision 19_GE8_049.
- This work was partly supported by the Institut Carnot ICEEL within the SOPRODSYSE and MATITHY projects.
- The authors would like to acknowledge contributions of the following:
  - The competence cluster on X-ray diffraction (CC-Xγ) at Institut Jean Lamour for providing advices in XRD measurements and analyses.
  - The competence cluster on electron microscopy (CC 3M) at Institut Jean Lamour for providing advices in SEM observations and EDX analyses.
  - The experimental facility Procédés from LEM3 (Université de Lorraine - CNRS UMR 7239) for providing advice in tribology measurements.

Data availability

The data that support the findings of this study are available from the corresponding author upon reasonable request.

Additional information

The authors declare no competing financial interests.

Contribution of each author

J. Martin, T. Czerwiec and G. Marcos conceptualized the goal of this research work.

J. Martin and G. Henrion conceived the PEO experimental rigs.

M.-P. Planche and H. Liao performed the sandblasting treatments and cold-spray depositions.

A. Maizeray and J. Martin performed the PEO experiments.

A. Maizeray and J. Martin performed the material characterizations.

A. Cappella and A. Maizeray performed the sliding wear tests.

A. Maizeray, J. Martin, T. Czerwiec and G. Marcos prepared the manuscript.

All the authors analysed the results and reviewed the manuscript.

T. Czerwiec, J. Martin, G. Marcos and G. Henrion supervised the whole work.

List of tables

Table 1: Elemental composition of the commercial 2017 grade aluminium alloy used as metallic substrate.

Composition	Cu	Mg	Mn	Fe	Si	Zn	Ti	Cr	Al
in wt%	3.9 – 5.0	0.5 – 1.2	0.4 – 1.2	0.3	0.5 – 1.2	0.25	0.15	0.1	Balance

Table 2: Elemental composition of the commercial 1050 grade aluminium alloy used as cold-sprayed powder.

Composition	Fe	Si	Zn	Cu, Mg, Mn, Ti	Al
in wt%	0.40	0.25	0.07	< 0.05	Balance

Table 3: Elemental composition of the corundum α-Al_2O_3 alumina used as cold-sprayed powder.

Composition	Fe_2O_3	Na_2O	SiO_2	CaO	Al_2O_3
in wt%	< 0.05	< 0.30	< 0.02	< 0.01	Balance

Table 4: Conditions of elaboration of the different samples using cold-spray (CS) and plasma electrolytic oxidation (PEO) processes. (Al is for the unsprayed Al2017 substrate and Al_PEO35min is for PEO of the unsprayed Al2017 substrate)

Sample name	Cold-spray deposition Al_2O_3 content (vol%)	PEO processing time (min)	PEO sparking regime
Al	-	-	-
CS0Al_2O_3	0	-	-
CS5Al_2O_3	5 ± 1	-	-
CS14Al_2O_3	14 ± 1	-	-
Al_PEO35min	-	35	soft
CS0Al_2O_3_PEO35min	0	35	soft
CS5Al_2O_3_PEO35min	5 ± 1	35	soft
CS14Al_2O_3_PEO20min	14 ± 1	20	arc
CS14Al_2O_3_PEO35min	14 ± 1	35	soft

Table 5: Morphological characteristics of the cold-sprayed and PEO coatings, and conditions of the dry sliding wear tests and the associated results. (Al is for the unsprayed Al2017 substrate and Al_PEO35min is for PEO of the unsprayed Al2017 substrate)

Sample name	Cold-spray coating		PEO coatings	Wear tests			
	Thickness (µm)	*Porosity (vol%)*	*Thickness (µm)*	*Normal load (N)*	*Sliding distance (m)*	*Average friction coef.*	*Wear rate (mm^3/(N·m)*
Al	-	-	-	1	10	0.63	$1.1\times10^{-3} \pm 4\times10^{-4}$
CS0Al_2O_3	420 ± 20	7 ± 0.5	-	1	10	0.89	$4.7\times10^{-3} \pm 4\times10^{-4}$
CS5Al_2O_3*	70 ± 10	3 ± 0.5	-	-	-	-	-
CS14Al_2O_3	280 ± 5	< 0.5	-	1	10	0.75	$7.0\times10^{-3} \pm 3\times10^{-4}$
Al_PEO35min	-	-	61 ± 5	7	50	0.72	$1.7\times10^{-5} \pm 5\times10^{-6}$
CS0Al_2O_3_PEO35min	420 ± 20	7 ± 0.5	72 ± 5	7	50	0.70	$2.4\times10^{-5} \pm 5\times10^{-6}$
CS5Al_2O_3_PEO35min*	70 ± 10	3 ± 0.5	48 ± 5	7	50	0.73	$6.4\times10^{-5} \pm 5\times10^{-6}$
CS14Al_2O_3_PEO20min	280 ± 5	< 0.5	23 ± 5	-	-	-	-
CS14Al_2O_3_PEO35min	280 ± 5	< 0.5	57 ± 5	7	50	0.65	$3.1\times10^{-5} \pm 2\times10^{-6}$

** Specific samples for which the thickness of the cold-spray coating (70 ± 10 µm) is close to the thickness of the PEO oxide layer (48 ± 5 µm)*

List of figures

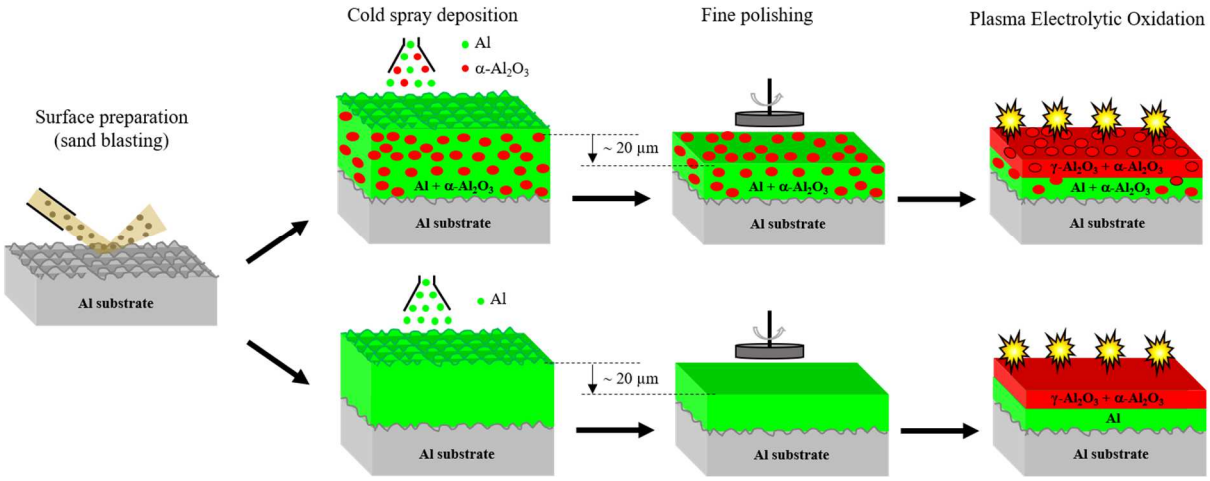

Figure 1: Schematic description of the duplex surface treatments carried out on aluminium substrate (prepared by sandblasting) consisting of, first, cold-spray deposition of an Al or an Al/α-Al_2O_3 composite coating followed by a fine polishing step (~ 20 µm thickness removal), and finally followed by plasma electrolytic oxidation (PEO).

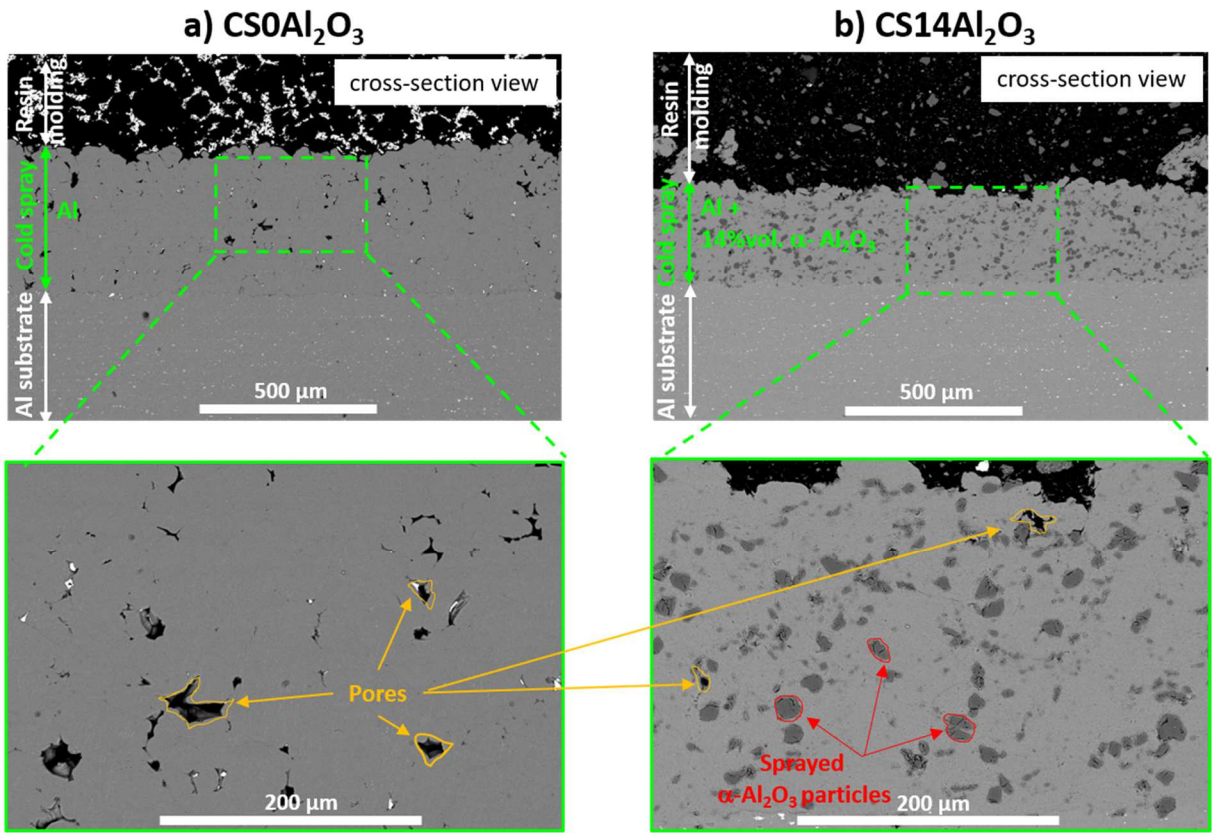

Figure 2: Cross-section SEM micrographs recorded in BSE imaging mode at different magnifications on the samples **a)** $CS0Al_2O_3$ and **b)** $CS14Al_2O_3$.

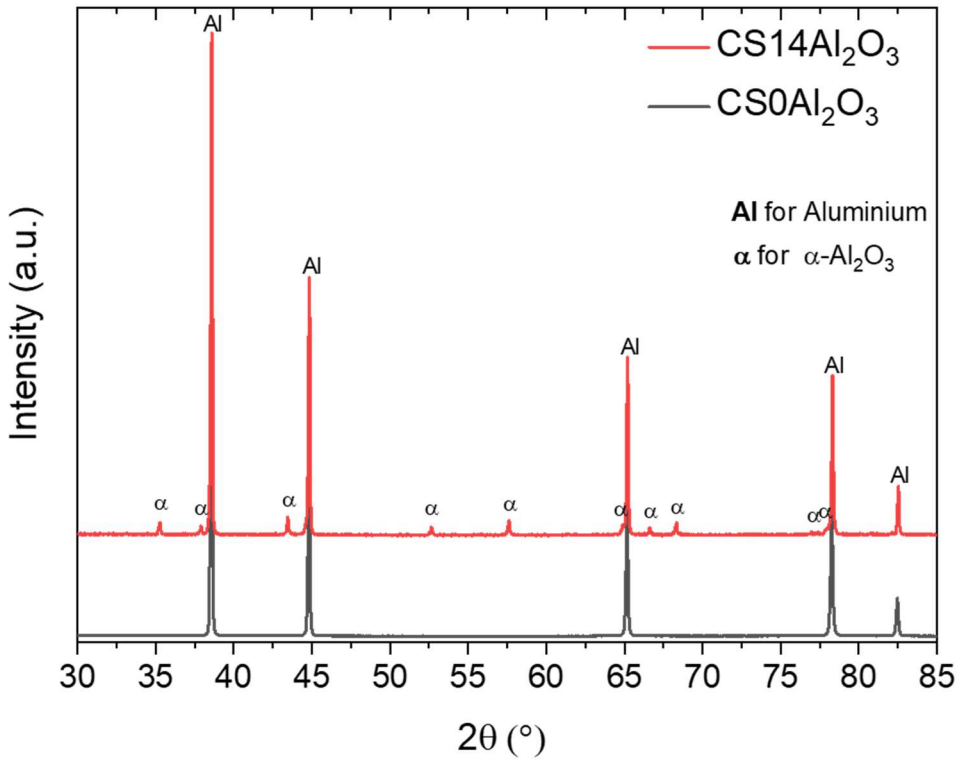

Figure 3: XRD diffraction patterns recorded in Bragg-Brentano geometry (Cu-$K_{\alpha 1}$ radiation λ = 0.1542 nm) on samples $CS0Al_2O_3$ and $CS14Al_2O_3$. Peak indexation is based on the JCPDS files, 00-004-0787 for the fcc-Al structure and 00-010-0173 for the rhombohedral α-Al_2O_3 structure.

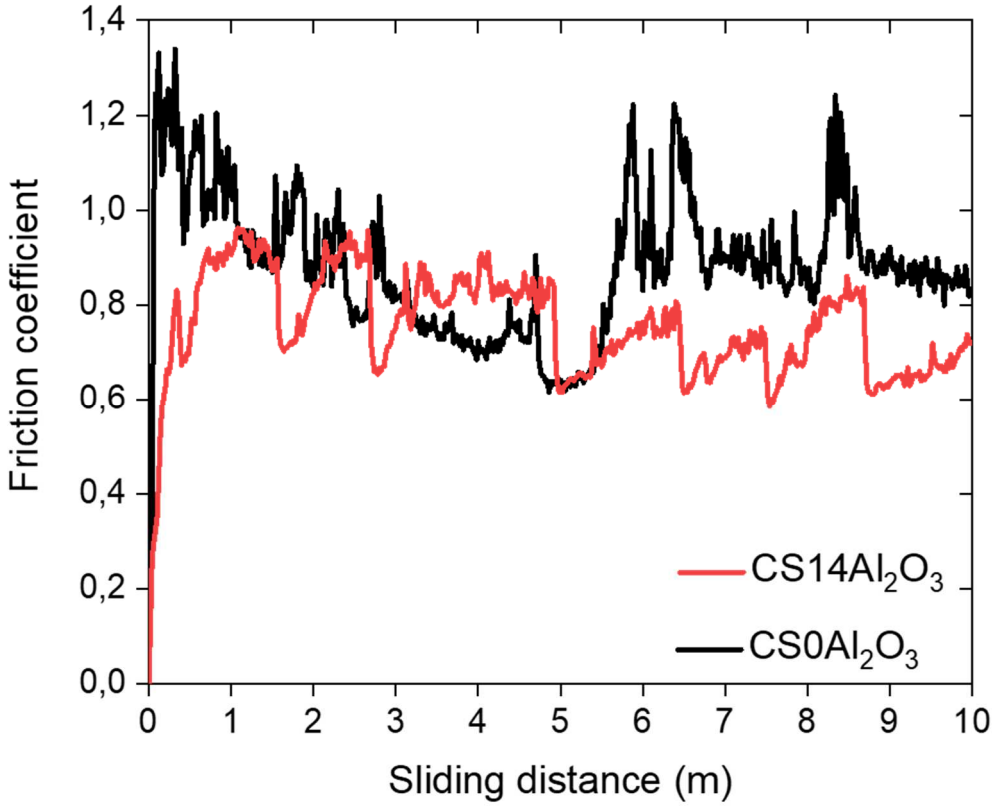

Figure 4: Variation of the friction coefficient as a function of the sliding distance recorded on the samples $CS0Al_2O_3$ and $CS14Al_2O_3$. Dry sliding wear tests were performed with a normal load of 1 N and a sliding distance of 10 m.

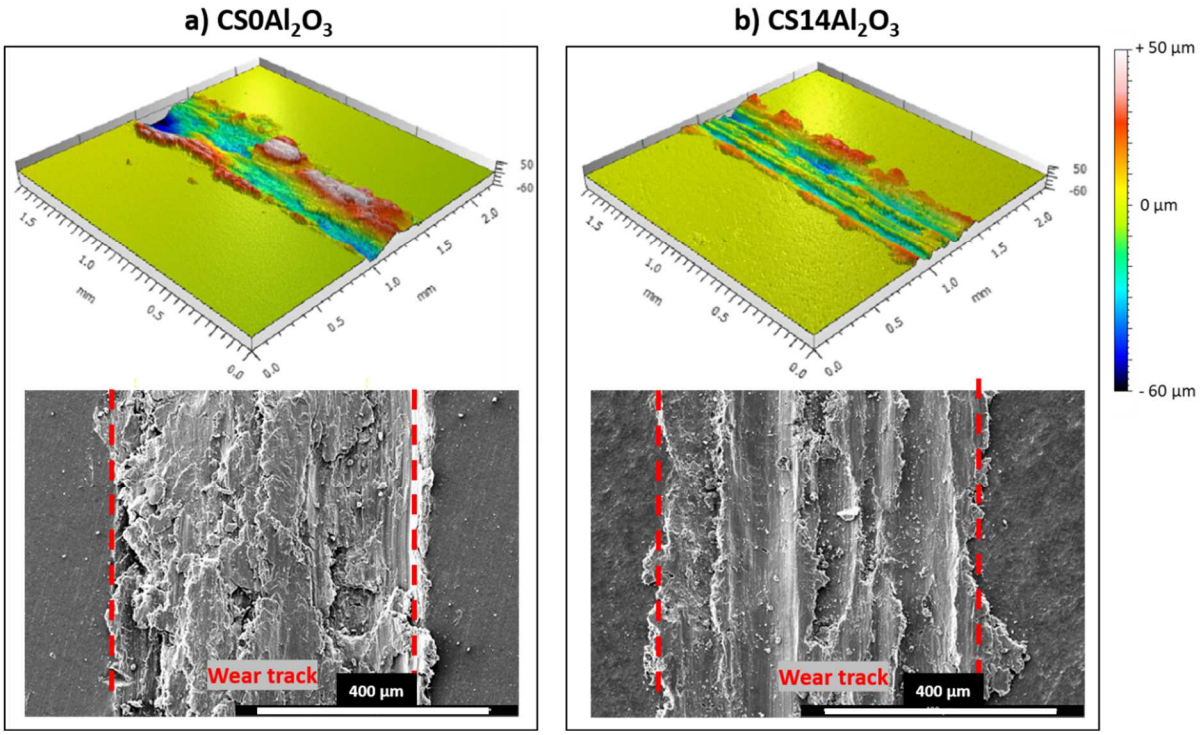

Figure 5: 3D images of the surface topography and the associated top-surface SEM micrographs recorded in SE imaging mode of the wear tracks obtained after dry sliding wear test performed on samples **a)** $CS0Al_2O_3$ and **b)** $CS14Al_2O_3$. Dry sliding wear tests were performed with a normal load of 1 N and a sliding distance of 10 m.

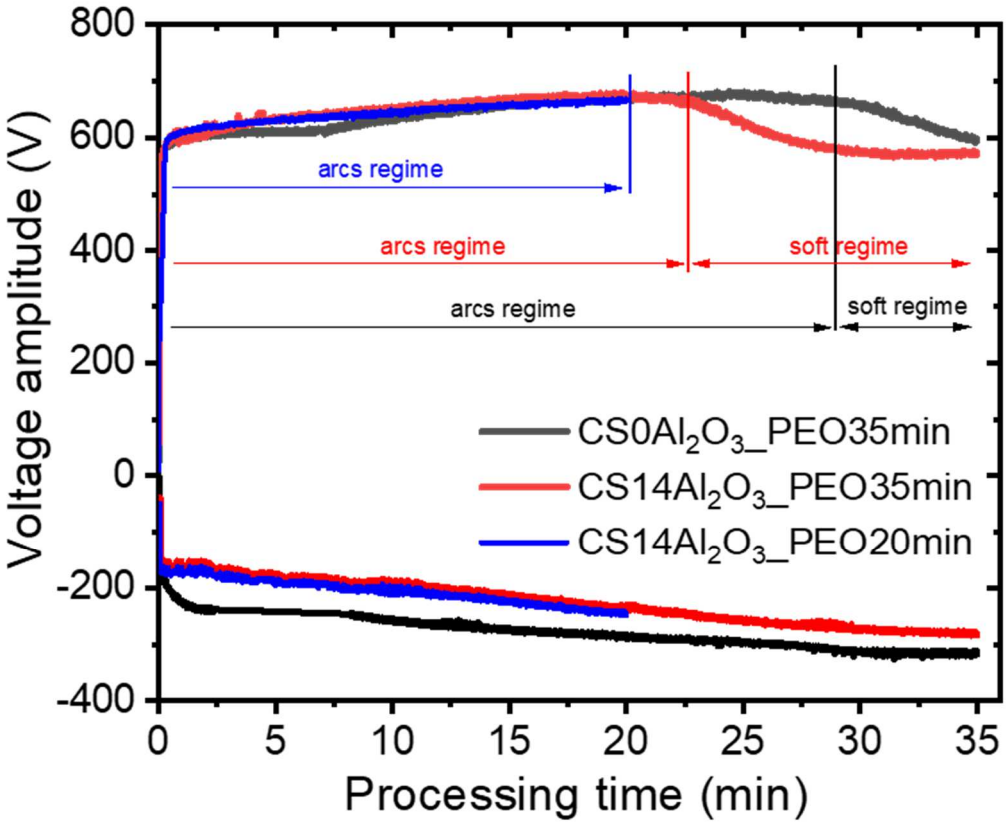

Figure 6: Voltage-time responses of the PEO treatments carried out for samples $CS0Al_2O_3$_PEO35min, $CS14Al_2O_3$_PEO20min and $CS14Al_2O_3$_PEO35min.

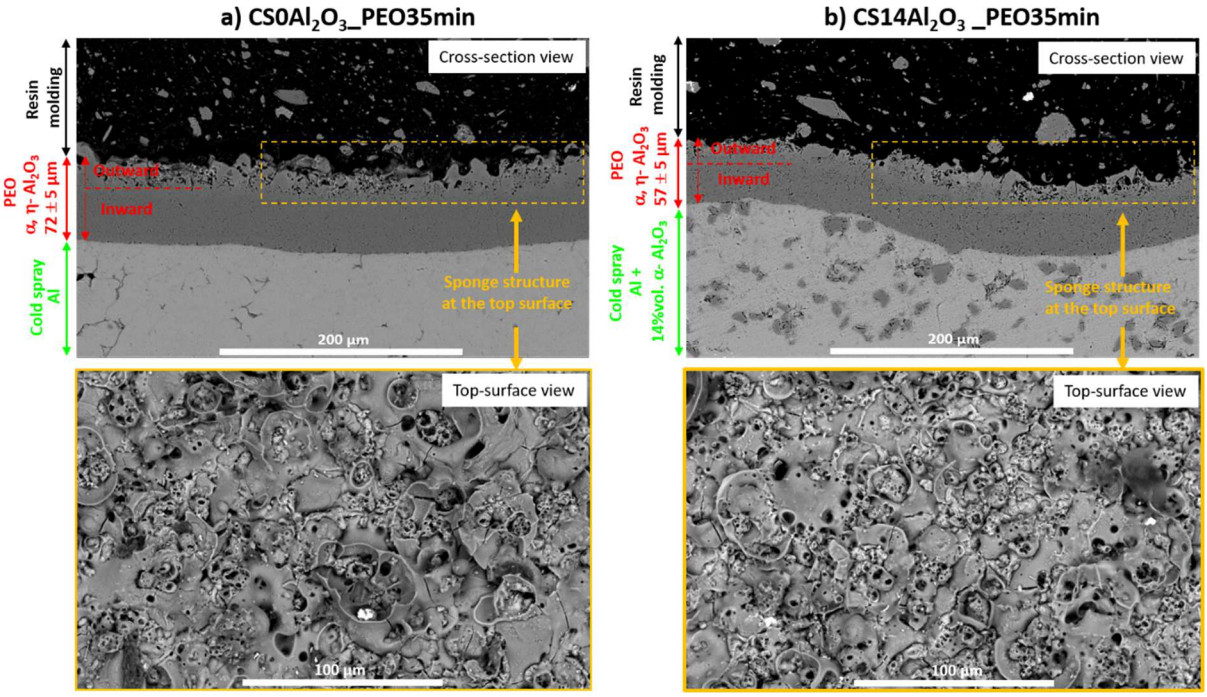

Figure 7: Cross-section and top-surface SEM micrographs recorded in BSE imaging mode on samples **a)** $CS0Al_2O_3$_PEO35min and **b)** $CS14Al_2O_3$_PEO35min.

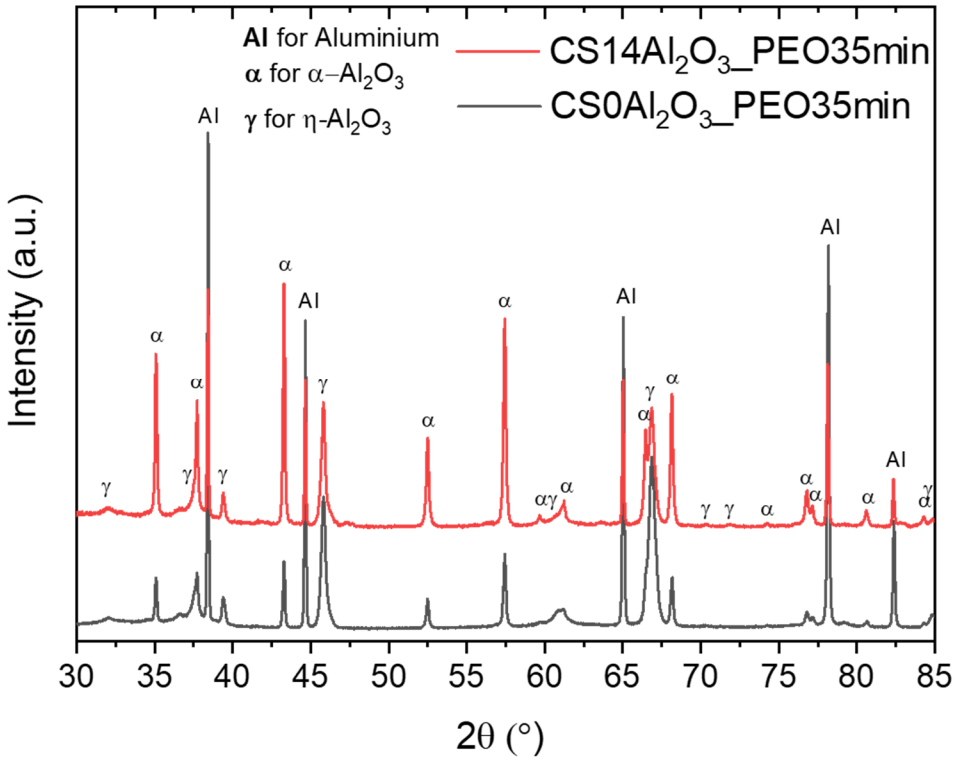

Figure 8: XRD diffraction patterns recorded in Bragg-Brentano geometry (Cu-$K_{\alpha 1}$ radiation λ = 0.1542 nm) on samples $CS0Al_2O_3$_PEO35min and $CS14Al_2O_3$_PEO35min. Peak indexation is based on the JCPDS files, 00-004-0787 for the fcc-Al structure, 00-010-0173 for the rhombohedral α-Al_2O_3 structure and 01-075-0921 for the fcc γ-Al_2O_3 structure.

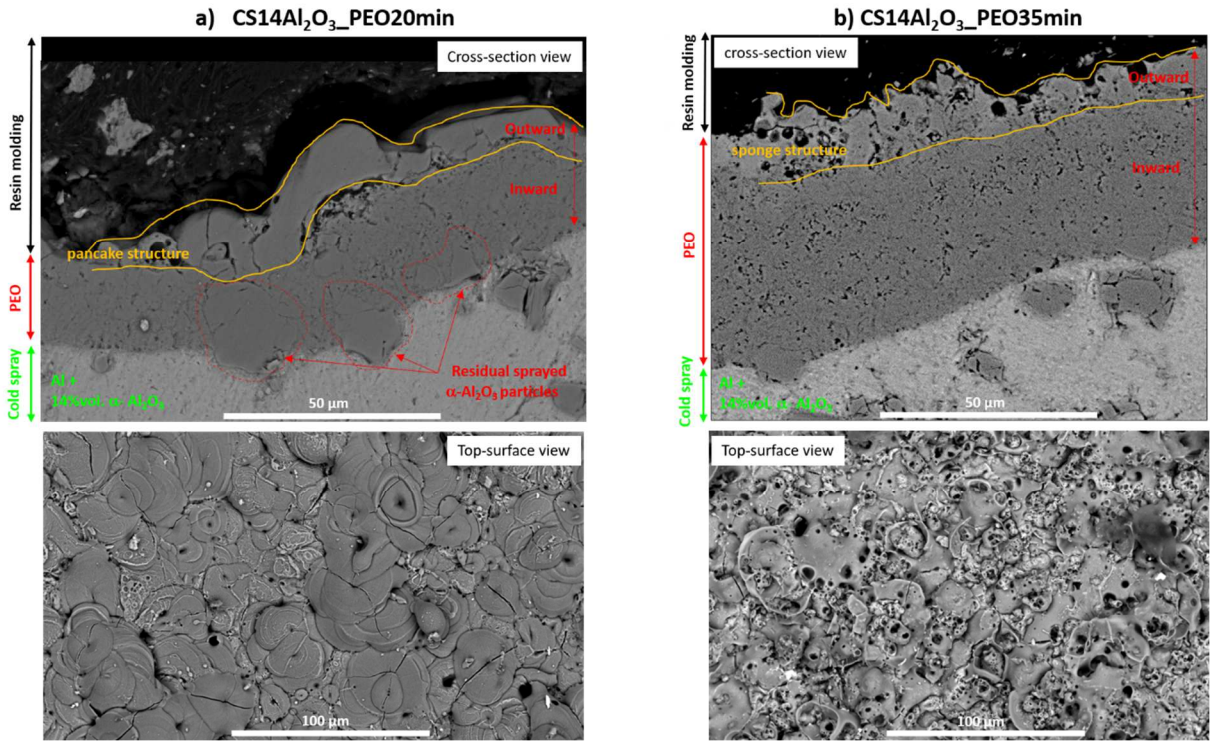

Figure 9: Cross-section and top-surface SEM micrographs recorded in BSE imaging mode on samples **a)** $CS14Al_2O_3$_PEO20min and **b)** $CS14Al_2O_3$_PEO35min.

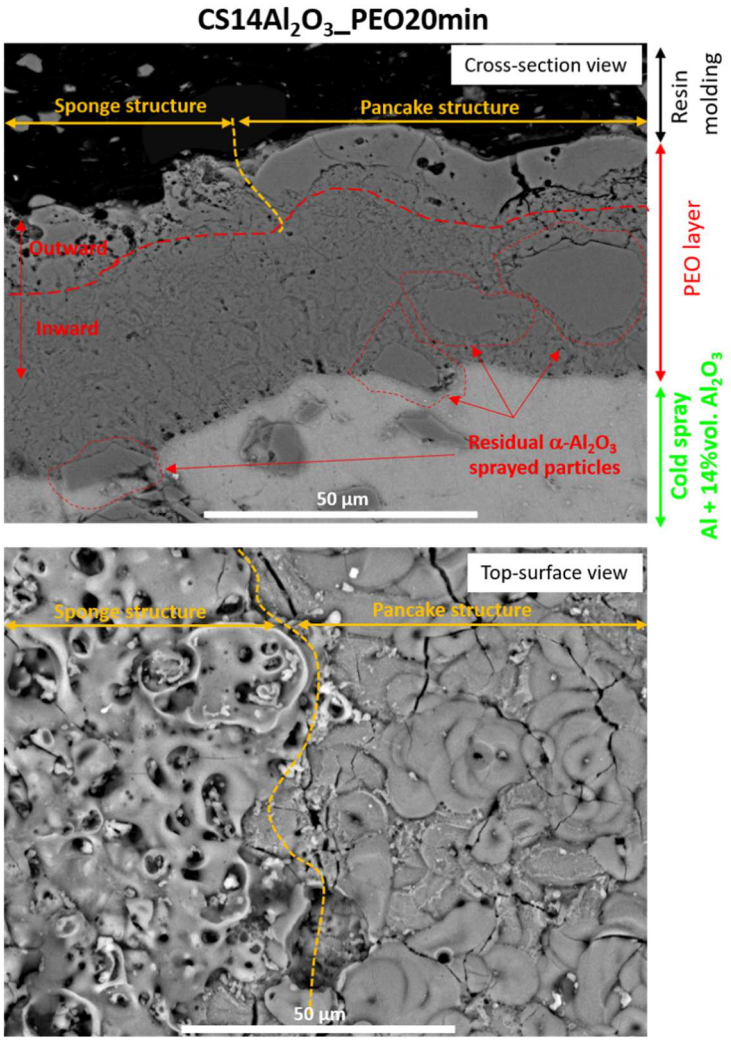

Figure 10: **a**) Cross-section and **b**) top-surface SEM micrographs recorded in BSE imaging mode on sample CS14Al$_2$O$_3$_PEO20min and showing the juxtaposition of a sponge-like morphology with a pancake-like morphology.

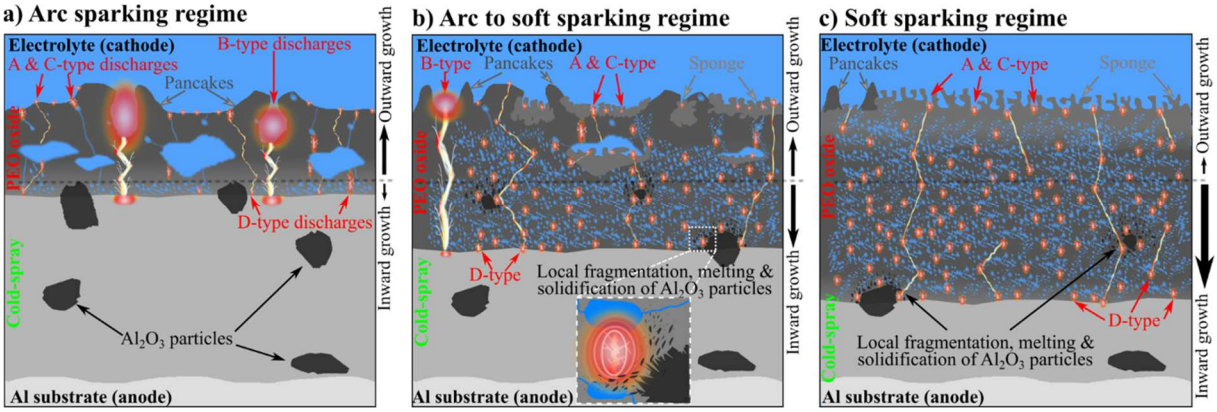

Figure 11: Schematic illustration of the gradual transformation of the dispersed α-Al_2O_3 particles into an aluminium cold-sprayed coating **a)** within the initial arc sparking regime, **b)** during the arc to soft sparking regime transition, and **c)** within the soft sparking regime.

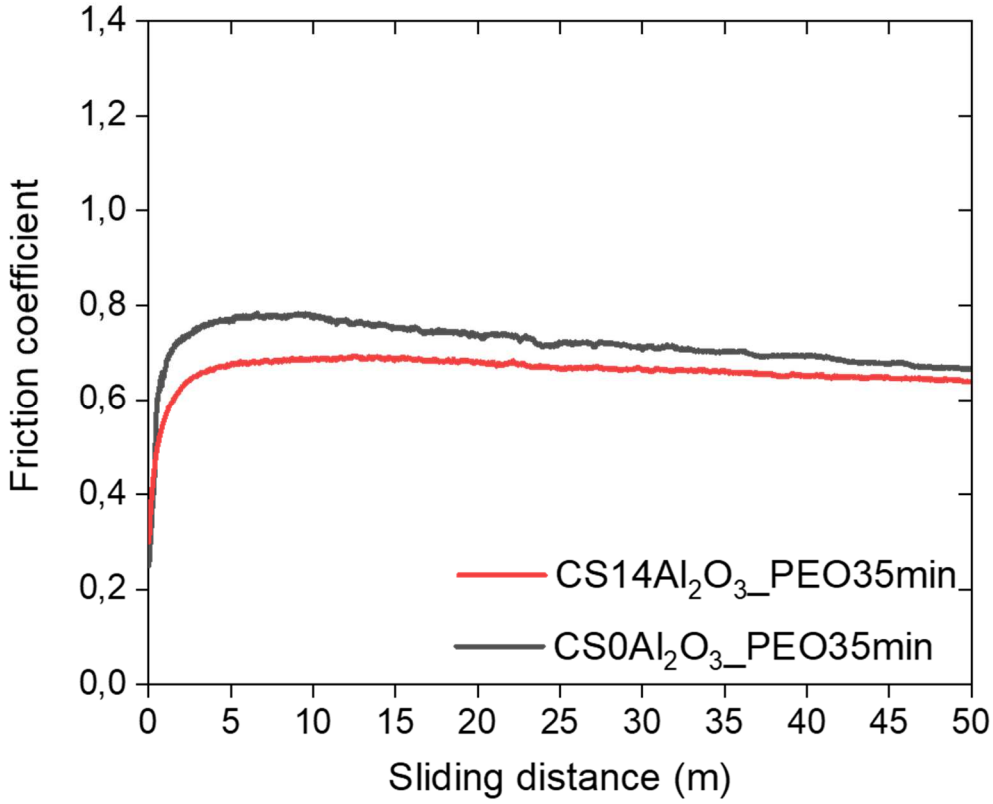

Figure 12: Variations of the friction coefficient as a function of the sliding distance recorded on samples $CS0Al_2O_3$_PEO35min and $CS14Al_2O_3$_PEO35min. Dry sliding wear tests were performed with a normal load of 7 N and a sliding distance of 50 m.

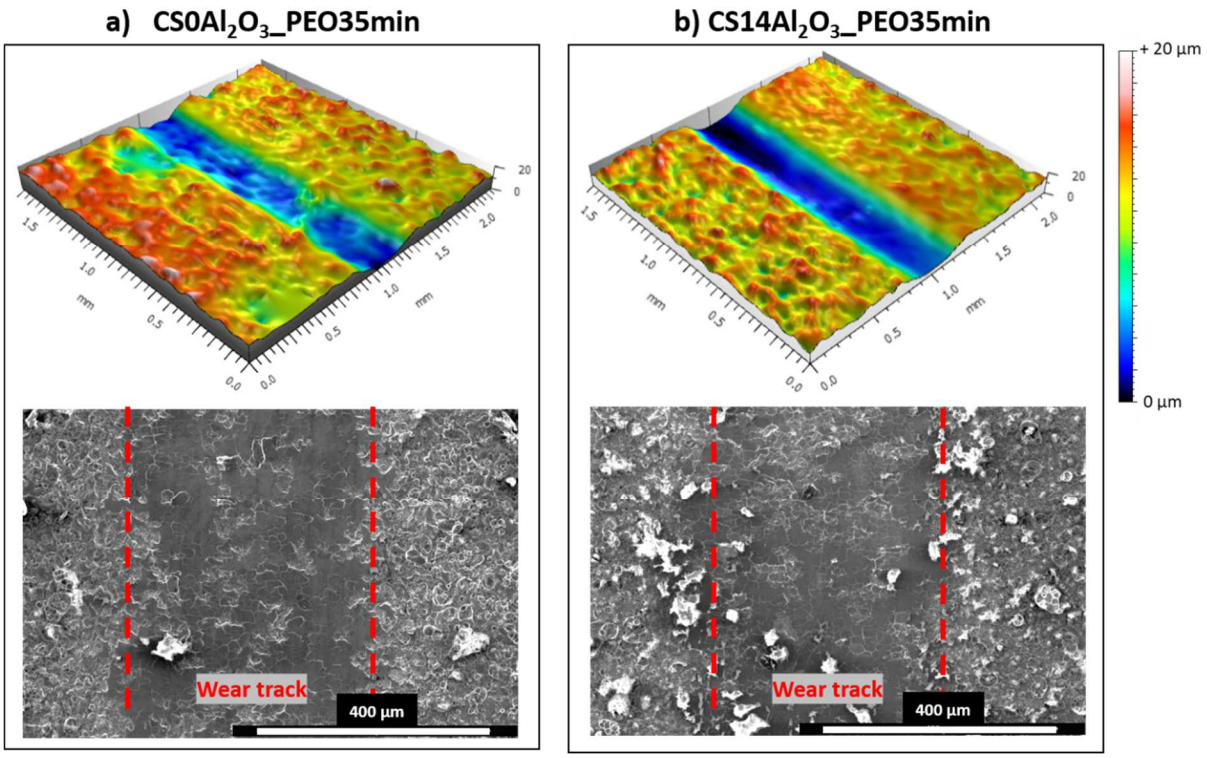

Figure 13: 3D images of the surface topography and the associated top-surface SEM micrographs recorded in SE imaging mode of the wear tracks obtained after dry sliding wear test performed on samples **a**) CS0Al_2O_3_PEO35min and **b**) CS14Al_2O_3_PEO35min. Dry sliding wear tests were performed with a normal load of 7N and a sliding distance of 50 m.

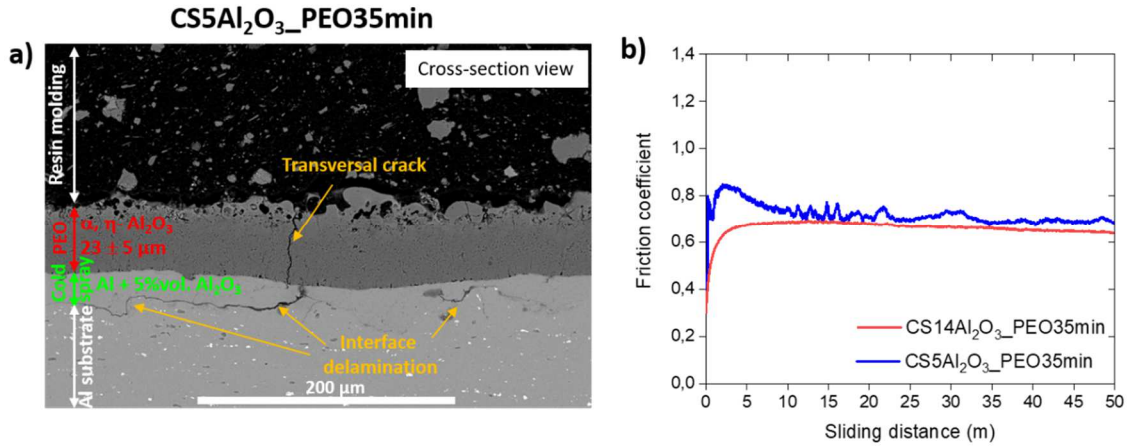

Figure 14: **a**) Cross-section SEM micrograph recorded in BSE imaging mode on sample $CS5Al_2O_3$_PEO35min. **b**) Variation of the friction coefficient as a function of the sliding distance recorded on samples $CS5Al_2O_3$_PEO35min and $CS14Al_2O_3$_PEO35min. Dry sliding wear tests were performed with a normal load of 7 N and a sliding distance of 50 m.